

# On the Application of the Briggs' and Steepest-Descent Methods to a Boundary-Layer Flow

*By R. J. Lingwood*

---

The evolution of wave packets generated by impulsive disturbances of the rotating-disk boundary-layer flow is studied. It is shown, by comparison with Briggs' method, that there are certain difficulties associated with the steepest-descent time-asymptotic method of evaluating the impulse response. The rotating-disk boundary layer provides examples of saddle points through which the steepest-descent path can and cannot be made to pass. It is shown that it is critically important to establish, from the topography of the phase function, whether the steepest-descent path passes through particular saddle points. If this procedure is not carried out, calculations of the wave-packet evolution can be majorly flawed and incorrect conclusions can be drawn about the stability of the flow, i.e., whether it is convectively or absolutely unstable.

---

## 1. Introduction

In this article, the impulsive disturbance of the incompressible rotating-disk boundary-layer flow is studied. A linear-stability analysis of this flow, for which there is an exact similarity solution of the Navier–Stokes equations [1] for the base flow, has been shown theoretically by Lingwood [2] to become

---

Address for correspondence: Dr. R. J. Lingwood, Department of Engineering, University of Cambridge, Trumpington Street, Cambridge CB2 1PZ, United Kingdom.

radially absolutely unstable for certain traveling waves above a critical Reynolds number,  $R$ , of about 510. Below this Reynolds number the flow is stable or convectively unstable depending on the parameters. The absolutely unstable nature of the flow has been confirmed experimentally by Lingwood [3] and it has been suggested that the absolute instability promotes the onset of nonlinearity and laminar–turbulent transition.

To discuss the evaluation of wave packets in this flow, it is necessary to describe the background to the problem; see Section 2. In Section 3 the solution to the inhomogeneous system is described. The major part of this description consists of a discussion of the inversion of the solution in spectral space to the physical domain; see Section 3.1. First, Briggs' method [4] is used to perform the inversion, followed by a description and comparison of the use of the steepest-descent method of inverting the solution. In Section 4 the steepest-descent method and a numerical-summation scheme are used to evaluate the wave-packet response to impulsive point disturbance to the boundary layer. Finally, in Section 5, some conclusions are drawn.

## 2. Background

In [2] with terms of  $O(R^{-2})$  neglected, the linearized sixth-order system of partial differential perturbation equations, which include viscous, Coriolis, and streamline-curvature terms, are reduced to a sixth-order system of ordinary differential equations by neglecting changes in Reynolds number with radius. Despite the fact that the rotating-disk boundary-layer thickness is constant, this sort of approximation is usually called the parallel-flow approximation and it implies that the results are restricted to the local stability characteristics of the flow. This system of equations is separable in radius,  $r$ , azimuthal angle,  $\theta$ , and time,  $t$ , and so the nondimensional perturbation quantities can be written in normal mode-form

$$\mathbf{u} = \hat{\mathbf{u}}(z; \alpha, \omega, \beta; R) e^{i(\alpha r + \beta \theta - \omega t)}, \quad (2.1)$$

where  $z$  is the axial coordinate and  $\mathbf{u} = (u, v, w)$  is the vector of perturbation velocities, in which the components refer to the radial, circumferential, and axial velocities, respectively; the perturbation pressure,  $p$ , can be written similarly. The angular perturbation frequency in a frame rotating with the disk is  $\omega$ , and  $\alpha$  and  $\beta$  are the radial and circumferential wavenumbers, respectively. Because of the periodic nature of the rotating-disk problem in the circumferential direction,  $\beta$  is an integer; in general,  $\alpha$  and  $\omega$  are complex. The real part of (2.1) is taken to obtain physical quantities. The local Reynolds number is  $R = r_s^* \Omega^* L^* / \nu^* = r_s^* / L^* = r_s$ , where the aster-

isks denote dimensional quantities,  $L^* = (\nu^* / \Omega^*)^{1/2}$  is the nondimensionalizing lengthscale,  $r_s^*$  is the radius at which the linear-stability analysis is applied,  $\Omega^*$  is the angular velocity of the disk, and  $\nu^*$  is the kinematic viscosity of the fluid. The nondimensionalizing velocity, pressure, and time scales are  $r_s^* \Omega^*$ ,  $\rho^* r_s^{*2} \Omega^{*2}$ , and  $L^* / (\Omega^* r_s^*)$ , respectively.

The governing perturbation equations may be written as a set of six first-order ordinary differential equations in the following transformed variables:

$$\phi_1(z; \alpha, \omega, \beta; R) = (\alpha - i/R)\hat{u} + \bar{\beta}\hat{v}, \quad (2.2)$$

$$\phi_2(z; \alpha, \omega, \beta; R) = (\alpha - i/R)\hat{u}' + \bar{\beta}\hat{v}', \quad (2.3)$$

$$\phi_3(z; \alpha, \omega, \beta; R) = \hat{w}, \quad (2.4)$$

$$\phi_4(z; \alpha, \omega, \beta; R) = \hat{p}, \quad (2.5)$$

$$\phi_5(z; \alpha, \omega, \beta; R) = (\alpha - i/R)\hat{v} - \bar{\beta}\hat{u}, \quad (2.6)$$

$$\phi_6(z; \alpha, \omega, \beta; R) = (\alpha - i/R)\hat{v}' - \bar{\beta}\hat{u}', \quad (2.7)$$

where  $\bar{\beta} = \beta/R$  and the prime represents differentiation with respect to  $z$ . These equations are

$$\phi_1' = \phi_2, \quad (2.8)$$

$$\begin{aligned} \phi_2' = & (\alpha^2 + \bar{\beta}^2 + iR(\alpha U + \bar{\beta}V - \omega) + U)\phi_1 + W\phi_2 \\ & + R((\alpha - i/R)U' + \bar{\beta}V')\phi_3 \\ & + iR(\alpha^2 + \bar{\beta}^2 - \alpha i/R)\phi_4 - 2(1 + V)\phi_5, \end{aligned} \quad (2.9)$$

$$\phi_3' = -i\phi_1, \quad (2.10)$$

$$R\phi_4' = iW\phi_1 - i\phi_2 - (\alpha^2 + \bar{\beta}^2 + iR(\alpha U + \bar{\beta}V - \omega) + W')\phi_3, \quad (2.11)$$

$$\phi_5' = \phi_6, \quad (2.12)$$

$$\begin{aligned} \phi_6' = & 2(1 + V)\phi_1 + R((\alpha - i/R)V' - \bar{\beta}U')\phi_3 + \bar{\beta}\phi_4 \\ & + (\alpha^2 + \bar{\beta}^2 + iR(\alpha U + \bar{\beta}V - \omega) + U)\phi_5 + W\phi_6. \end{aligned} \quad (2.13)$$

This system has six independent solutions  $\phi_i^j(z; \alpha, \omega, \beta; R)$  ( $i = j = 1, 2, 3, \dots, 6$ ), where the subscript  $i$  indicates one of the six transformed

variables and the superscript  $j$  indicates one of the six solutions. Moreover, Equations (2.8)–(2.13) in the limit  $z \rightarrow \infty$  have exact closed-form solutions that are exponential in form:

$$\phi_i^j(z \rightarrow \infty; \alpha, \omega, \beta; R) = c_i^j e^{\kappa_j z}, \quad i = j = 1, 2, 3, \dots, 6, \quad (2.14)$$

where  $c_i^j$  represents a constant coefficient. The values of  $\kappa_j$  are

$$\kappa_{1,2} = \kappa_{3,4} = W_\infty/2 \mp \left( (W_\infty/2)^2 + \gamma^2 - iR(\bar{\beta} + \omega) \right)^{1/2}, \quad (2.15)$$

$$\kappa_{5,6} = \mp (\gamma^2 - \alpha i/R)^{1/2}, \quad (2.16)$$

where  $W(z \rightarrow \infty) \equiv W_\infty \approx -0.8838$  and  $\gamma^2 = \alpha^2 + \bar{\beta}^2$ . The real part of all complex square roots is taken to be positive. This choice is equivalent to introducing a branch cut along the negative real axis in the complex  $S$ -plane, where  $S$  is the function to be square rooted. Of course, the branch cut in the  $S$ -plane could be chosen differently but, as discussed by Ashpis and Reshotko [5], any other choice would complicate the solution. Letting  $S_1 = (W_\infty/2)^2 + \gamma^2 - iR(\bar{\beta} + \omega)$ , then (2.15) becomes  $\kappa_{1,2} = \kappa_{3,4} = W_\infty/2 \mp \sqrt{S_1}$ . For fixed  $R$ ,  $\beta$ , and  $\omega$ , the branch cut along the negative real axis in the  $S_1$ -plane is mapped to two hyperbolic branch cuts in the complex  $\alpha$ -plane, which ensure that  $\Re(\sqrt{S_1}) > 0$  for all values of  $\alpha$  and  $\omega$ . The two hyperbolic branch cuts in the  $\alpha$ -plane end in branch points that are given by  $S_1 = 0$ . Figure 1a shows a sketch of the branch cuts in the  $\alpha$ -plane, for positive  $\beta$ ,  $\omega_r$ , and  $\omega_i$ . The branch points in the upper- and lower-half planes are given by  $BP_{1u,l} = \pm (iR(\bar{\beta} + \omega) - \bar{\beta}^2 - (W_\infty/2)^2)^{1/2}$ . Similarly, letting  $S_2 = \gamma^2 -$

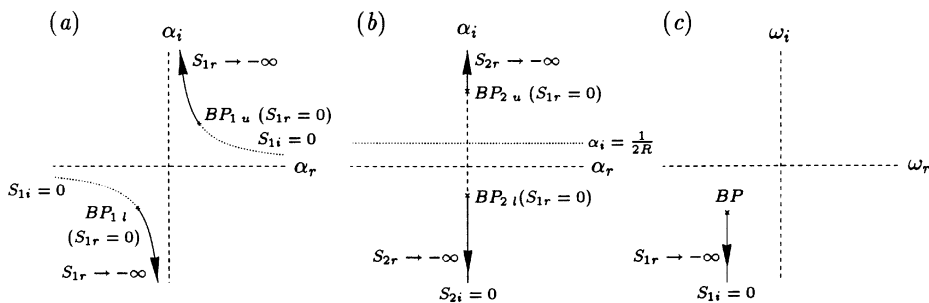


Figure 1. (a) Sketch of the hyperbolic branch cuts (—) in the  $\alpha$ -plane. The branch points in the upper- and lower-half planes are given in the text. (b) Sketch of the imaginary-axis branch cuts (—) in the  $\alpha$ -plane. The branch points in the upper- and lower-half planes are given in the text. (c) Sketch of the branch cut (—) in the  $\omega$ -plane. The expression for  $BP$  is given in the text.

$\alpha i/R$ , (2.16) becomes  $\kappa_{5,6} = \mp \sqrt{S_2}$ . For fixed  $R$ ,  $\beta$ , and  $\omega$ , the cut along the negative real axis in the  $S_2$ -plane maps to parts of the imaginary  $\alpha$ -axis. The cuts are symmetric about the line  $\alpha_i = 1/(2R)$  (henceforth, the subscripts  $r$  and  $i$  refer to real and imaginary parts, respectively) and the values of the branch points are  $BP_{2u,l} = i/(2R)(1 \pm (1 + 4\beta^2 R^2)^{1/2})$ . Figure 1b shows a sketch of the branch cuts in the  $\alpha$ -plane. Unlike  $S_2$ ,  $S_1$  is dependent on  $\omega$ . For fixed  $R$ ,  $\beta$ , and  $\alpha$ , the branch cut along the negative real axis in the  $S_1$ -plane is also mapped to a cut in the complex  $\omega$ -plane, again ensuring that  $\Re(\sqrt{S_1}) > 0$  for all values of  $\alpha$  and  $\omega$ . The value the branch point in the  $\omega$ -plane is  $BP = -\bar{\beta} - i((W_\infty/2)^2 + \gamma^2)/R$ . Note that for real  $\alpha$  the bracketed term is purely real. Figure 1c shows a sketch of the branch cut in the  $\omega$ -plane, for positive  $\beta$  and real  $\alpha$ .

The solution to (2.8)–(2.13) is formed by summing the six fundamental solutions, with appropriate weightings, in such a way that the boundary conditions are satisfied. Components of the final solution vector are represented by

$$\phi_i(z; \alpha, \omega, \beta; R) = \sum_{j=1}^6 C_j(\alpha, \omega, \beta; R) \phi_i^j(z; \alpha, \omega, \beta; R),$$

$$i = 1, 2, 3, \dots, 6, \quad (2.17)$$

where  $C_j(\alpha, \omega, \beta; R)$ , which is constant with respect to  $z$ , is the weighting coefficient of the  $j$ th solution vector.

In [2] the time-asymptotic response is sought to an impulsive circumferential line forcing, with prescribed integer  $\beta$ , such that the axial velocity at  $z = 0$  is given by

$$w(0; r, \theta, t) \equiv \phi_3(0; r, \theta, t) = \delta(r - r_s) \delta(t) e^{i\beta\theta}, \quad (2.18)$$

where  $\delta(r - r_s)$  and  $\delta(t)$  are the Dirac delta functions at a nondimensional radius of  $r_s$  and at  $t = 0$ , respectively. The response to point forcing can be obtained by summing over all integer values of  $\beta$ . The additional boundary conditions at  $z = 0$ , given by the no-slip condition, are

$$u(0; r, \theta, t) = v(0; r, \theta, t) = 0, \quad (2.19)$$

and as  $z \rightarrow \infty$  it is required that all perturbations decay.

### 3. Solution of the inhomogeneous system

The governing perturbation equations (2.8)–(2.13) are in the Fourier domain. Therefore, it is necessary to take Fourier transforms of the boundary

conditions and then to take inverse transforms of the results to recover solutions in the physical domain. For initial-value problems of this sort, disturbances are limited in space at any finite time, because they are generated at some initial instant and propagate at finite velocities. Therefore, the flow is always undisturbed sufficiently far from the source ( $|r - r_s| \rightarrow \infty$ ) at any fixed time. Because of this, the Fourier transform with respect to  $r$  at fixed  $t$  exists with  $\alpha$  real, and the subsequent inverse wavenumber transform (see Section 3.1) can be taken along the real  $\alpha$ -axis. In fact, there is a strip of analyticity in the complex  $\alpha$ -plane, which includes the real axis, within which the inversion contour can lie. In contrast, the Fourier transform with respect to  $t$  does not exist for real  $\omega$  if there are instabilities that grow exponentially as  $t \rightarrow \infty$ . However, since the forcing is causal, the transform must be zero for  $t < 0$  and the Fourier transform with respect to  $t$  can be taken provided  $\omega$  has positive imaginary part greater than any of the growth rates associated with any possible temporal instabilities. The implication is that provided the subsequent frequency inversion is taken along a contour above all the singularities in the  $\omega$ -plane, both convergence of the direct Fourier transform and causality of the inverse transform are guaranteed. Accordingly, using the axial velocity component as an example, the boundary conditions are represented in Fourier space by

$$\hat{w}(z; \alpha, \omega; \beta, R) = e^{i\beta\theta} \int_{-\infty}^{+\infty} \int_{-\infty}^{+\infty} w(z; r, \theta, t) e^{-i(\alpha r - \omega t)} dr dt, \quad (3.1)$$

where  $\alpha$  is real and  $\omega$  is complex, with an imaginary part larger than that of all singularities in the  $\omega$ -plane.

The lower limit of the time integration could be replaced by zero because  $w$  is a causal function in  $t$ . Therefore the integrand is identically zero for  $t < 0$ , and (3.1) is equivalent to a Laplace–Fourier transform. Clearly, the zero physical boundary conditions at the wall transform to zero spectral boundary conditions for  $\hat{u}$  and  $\hat{v}$  and it follows from (2.18) and (3.1) that

$$\hat{w}(0; \alpha, \omega; \beta, R) = e^{i(\beta\theta - \alpha r_s)}. \quad (3.2)$$

The boundary conditions together with the governing perturbation equations form an inhomogeneous system, where the inhomogeneity is introduced in the boundary condition (3.2). A similar approach has been used by Ashpis and Reshotko [5] and Gaster [6], among others. The inhomogeneity could have been included in the perturbation equations, as by Gustavsson [7], but for a three-dimensional boundary layer this approach is more difficult and is not pursued here.

The requirement that the disturbances vanish as  $z \rightarrow \infty$  implies  $C_2 = C_4 = C_6 = 0$ . Values of  $C_1$ ,  $C_3$ , and  $C_5$  are determined from the boundary conditions at  $z = 0$  and can be written as

$$\begin{pmatrix} \phi_1(0) \\ \phi_3(0) \\ \phi_5(0) \end{pmatrix} = \begin{pmatrix} \phi_1^1(0) & \phi_1^3(0) & \phi_1^5(0) \\ \phi_3^1(0) & \phi_3^3(0) & \phi_3^5(0) \\ \phi_5^1(0) & \phi_5^3(0) & \phi_5^5(0) \end{pmatrix} \begin{pmatrix} C_1 \\ C_3 \\ C_5 \end{pmatrix} = \begin{pmatrix} 0 \\ \hat{f} \\ 0 \end{pmatrix}, \quad (3.3)$$

where  $\hat{f} = e^{i(\beta\theta - \alpha r_s)}$  from Equation (3.2) and the dependence on  $\beta$ ,  $R$ ,  $\alpha$ , and  $\omega$  has been omitted from the list of variables. Letting the Wronskian be  $\Delta_0(\alpha, \omega; \beta, R)$ , Cramer's rule gives

$$C_1 = \Delta_1 \hat{f} / \Delta_0, \quad \Delta_1 = \phi_5^3(0) \phi_1^5(0) - \phi_1^3(0) \phi_5^5(0), \quad (3.4)$$

$$C_3 = \Delta_3 \hat{f} / \Delta_0, \quad \Delta_3 = \phi_1^1(0) \phi_5^5(0) - \phi_5^1(0) \phi_1^5(0), \quad (3.5)$$

$$C_5 = \Delta_5 \hat{f} / \Delta_0, \quad \Delta_5 = \phi_5^1(0) \phi_1^3(0) - \phi_1^1(0) \phi_5^3(0). \quad (3.6)$$

Therefore, using (2.17), the result for  $\phi_i(z; \alpha, \omega; \beta, R)$  is

$$\phi_i(z) = \hat{f} (\Delta_1 \phi_i^1(z) + \Delta_3 \phi_i^3(z) + \Delta_5 \phi_i^5(z)) / \Delta_0, \quad i = 1, 3, 5. \quad (3.7)$$

### 3.1. Inversion to the physical domain

Singularities of  $\phi_i(z; \alpha, \omega; \beta, R)$  are important to the inversion of solution (3.7) to the physical domain. Singularities occur for two reasons: due to the branch cuts in the  $\alpha$ - and  $\omega$ -planes, which map from the complex  $S$ -plane associated with the square roots in (2.15) and (2.16), and due to zeros of  $\Delta_0(\alpha, \omega; \beta, R)$ . The branch cuts cause continuous singularities and the zeros of  $\Delta_0(\alpha, \omega; \beta, R)$  cause discrete singularities. If the branch cuts in the  $S$ -plane were chosen differently, the categorization of singularities may change; i.e., what was a singularity in the discrete spectrum may become part of a continuous spectrum and vice versa. Note that zeros of  $\Delta_0(\alpha, \omega; \beta, R)$  are the only nontrivial solutions to the homogeneous problem (the unforced case), given by (3.3) with zero right-hand side. Furthermore, zeros of the Wronskian define the so-called dispersion relation, and combinations of  $\omega$ ,  $\alpha$ , and  $\beta$  (for given  $R$ ) that satisfy the dispersion relation are discrete eigenvalues, with associated eigenfunctions. The discrete eigenvalues provide a mapping between the  $\alpha$ - and  $\omega$ -plane, such that zeros of the

dispersion relation in the  $\alpha$ -plane are given by

$$\alpha = \alpha_j(\omega, \beta; R), \quad j = 1, \dots, M, \quad (3.8)$$

and in the  $\omega$ -plane zeros are given by

$$\omega = \omega_j(\alpha, \beta; R), \quad j = 1, \dots, N, \quad (3.9)$$

where  $M$  and  $N$  are the number of discrete modes in the  $\alpha$ - and  $\omega$ -plane, respectively. Discrete eigenvalues trace out paths in the  $\alpha$ -plane ( $\omega$ -plane) as  $\omega$  ( $\alpha$ ) is varied. Note that the governing equations (2.8)–(2.13) have a symmetry property, whereby  $\alpha_j(\omega, \beta; R) \mapsto -\alpha_j^*(-\omega^*, -\beta^*; R)$  and  $\omega_j(\alpha, \beta; R) \mapsto -\omega_j^*(-\alpha^*, -\beta^*; R)$ , where the asterisks indicate the complex conjugate. Thus, trajectories of the dispersion relation given by (3.8) for  $\omega_r < 0$  and  $\beta_r < 0$  are symmetric with respect to the imaginary  $\alpha$ -axis to those for  $\omega_r > 0$  and  $\beta_r > 0$ . Similarly, trajectories given by (3.9) for  $\alpha_r < 0$  and  $\beta_r < 0$  are symmetric about the imaginary  $\omega$ -axis to those for  $\alpha_r > 0$  and  $\beta_r > 0$ .

Inversion of  $\phi_3(z; \alpha, \omega; \beta, R)$  is used as an example. Inversion of  $\phi_1(z; \alpha, \omega; \beta, R)$  and  $\phi_5(z; \alpha, \omega; \beta, R)$  is similar, but  $\phi_1$  and  $\phi_5$  need to be considered together to recover  $u(z; r, \theta, t)$  and  $v(z; r, \theta, t)$ . The following double inverse Fourier transform defines  $w(z; r, \theta, t)$ :

$$w(z; r, \theta, t) = \frac{1}{(2\pi)^2} \int_F \int_A \phi_3(z; \alpha, \omega; \beta, R) e^{i(\alpha r - \omega t)} d\alpha d\omega, \quad (3.10)$$

and it follows from (3.7) that

$$w(z; r, \theta, t) = \frac{e^{i\beta\theta}}{(2\pi)^2} \int_F \int_A \frac{\Phi(z; \alpha, \omega; \beta, R)}{\Delta_0(\alpha, \omega; \beta, R)} e^{i(\alpha(r-r_s) - \omega t)} d\alpha d\omega, \quad (3.11)$$

where  $F$  and  $A$  are the inversion contours in the  $\omega$ - and  $\alpha$ -planes, respectively, and  $\Phi = \Delta_1 \phi_3^1(z; \alpha, \omega; \beta, R) + \Delta_3 \phi_3^3(z; \alpha, \omega; \beta, R) + \Delta_5 \phi_3^5(z; \alpha, \omega; \beta, R)$ . The two transforms are dependent on each other. Assuming it is acceptable to reverse the order of integration, then if the  $\alpha$ -inversion is performed first,  $\omega$  becomes a parameter, the values of which are determined by the  $F$ -contour. Equally, if the  $\omega$ -inversion is performed first, then  $\alpha$  is the parameter, which is determined by the  $A$ -contour.

Both inversion contours must lie in regions of analyticity in the respective complex planes. Therefore, the contours must avoid the continuous singularities and discrete singularities. If the inversion contours are incorrectly taken



through regions of nonanalyticity, the inversion can still be formally carried out but, as well as being noncausal, the solution may not converge to a solution of the problem at hand. In the  $\alpha$ -plane there is a strip of analyticity, centered on the line  $\alpha_i = 1/(2R)$  and including the real axis; see Figure 1b. The strip of analyticity always has nonzero width. (Note that the  $\omega$ -dependent hyperbolic branch cuts in the  $\alpha$ -plane always lie in the distinct half  $\alpha$ -planes.) Taking the  $A$ -contour along the real  $\alpha$ -axis gives purely temporal branches of the dispersion relation in the  $\omega$ -plane. The region of analyticity in the  $\omega$ -plane lies above, and includes, the horizontal  $F$ -contour (sometimes referred to as the Bromwich contour), which must lie above all the discrete singularities and branch cuts given by the  $A$ -contour, for a zero response at  $t < 0$ . The relevant branch cut in the  $\omega$ -plane is given typically by Figure 1c and always lies below the real  $\omega$ -axis when  $\alpha$  is real. The  $F$ -contour produces branches in the  $\alpha$ -plane that are not purely spatial since they have complex  $\omega$ , with positive  $\omega_i$ . Nonetheless, any branch of the dispersion relation given by a predetermined  $\omega$ -distribution is referred to as a spatial branch; similarly, any branch that lies in the  $\omega$ -plane and is given by a predetermined  $\alpha$ -distribution, which may be complex, will be called a temporal branch. With  $\omega_i$  above any singularities in the  $\omega$ -plane, the spatial branches do not cross the real  $\alpha$ -axis and they correspond to spatially damped eigenvalue solutions. It follows that any branch lying in the upper-half  $\alpha$ -plane leads to a response in the physical region  $r > r_s$ , while any branch lying in the lower-half  $\alpha$ -plane corresponds to the region  $r < r_s$ . The above choice of contours ensures convergence of the transforms and satisfies causality.

**3.1.1. Briggs' method.** In principle, Equation (3.11) can be determined for all  $r$  and  $t$ , but the complexity of the dispersion relationship means that it is easier to calculate the time-asymptotic solution. In [2], Briggs' method [4] was used to distinguish between convectively and absolutely unstable time-asymptotic responses, but the details of the method were not given. Here, it is necessary to outline this solution method so that comparisons can be drawn with the method of steepest descent, which is discussed in Section 3.1.2.

In Briggs' method the wavenumber integral is chosen as the first Fourier inversion and is given by

$$\tilde{w} = \frac{1}{2\pi} \int_A \frac{\phi}{\Delta_0} e^{i(\alpha(r-r_s))} d\alpha. \quad (3.12)$$

This is followed by the  $\omega$ -inversion, given by

$$w = \frac{e^{i\beta\theta}}{2\pi} \int_F \tilde{w} e^{-i\omega t} d\omega. \quad (3.13)$$

The method of analytic continuation is used to deflect the original  $F$ -contour, illustrated by Figure 2a onto the  $F'$ -contour, shown in Figure 2b, in an attempt to lower the contour to just below the real  $\omega$ -axis. If this is achieved, the exponent in (3.13) forces the integrand to vanish as  $t \rightarrow \infty$ ; if not the time-asymptotic discrete response is governed by the highest discrete singularity in the  $\omega$ -plane. If the  $A$ -contour, on the real  $\alpha$ -axis, gives an unstable temporal branch, as shown in Figure 2a, then lowering the  $F$ -contour to the real axis would violate causality and there would be a loss of analyticity on the  $F$ -contour. Therefore, the  $A$ -contour must be simultaneously deformed off the real  $\alpha$ -axis (such that the contour still passes on the correct side of the spatial branches) onto the  $A'$ -contour, causing the temporal branch to lie lower in the  $\omega$ -plane (below the  $F'$ -contour), as shown in Figure 2b. The response is zero for  $t < 0$  above the  $F'$ -contour and so causality and analyticity are satisfied and the inversion integrals (3.12) and (3.13) can be redefined for the deformed contours. The branch cuts are not shown in Figure 2 because they do not interfere with the deflection process; the hyperbolic cuts in the  $\alpha$ -plane do not cross the real axis, the imaginary-axis cuts are independent of  $\omega$ , and, provided  $\alpha_r^2 + \bar{\beta}^2 + (W_\infty/2)^2 > \alpha_i^2$ , deflecting the  $A$ -contour off the real axis does not cause the cut in the  $\omega$ -plane to cross into the upper-half plane. Note that for a spatial branch to cross the real  $\alpha$ -axis for some value of  $\omega$  on the  $F'$ -contour, part of a temporal branch must lie in the upper-half  $\omega$ -plane for some value of real  $\alpha$ , i.e., for

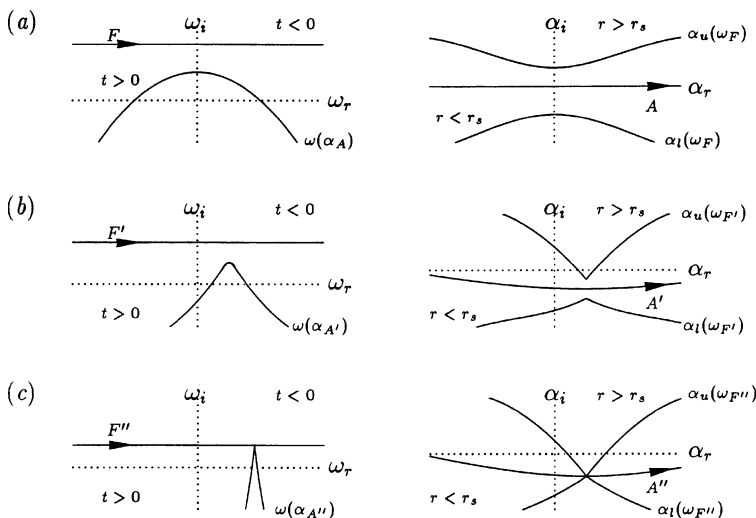


Figure 2. Sketches of a temporal branch of the dispersion relation given by the  $A$ -contour and spatial branches given by the  $F$ -contour: (a), (b) and (c) represent lowering the  $F$ -contour and the deformation of the  $A$ -contour until the pinching condition occurs. The subscripts u and l refer to upper- and lower-half  $\alpha$ -planes, respectively.

some part of the original  $A$ -contour. Thus, temporal instability implies spatial instability, unless the boundary conditions of the problem constrain the wavenumber to be real (e.g., the Taylor–Couette flow), in which case the flow can have a temporal instability but no spatial instability.

An essential part of Briggs' method is to check whether two or more poles of the integrand in (3.12) (zeros of the dispersion relation) from different sides of the  $A$ -contour coalesce, such that for a particular value of  $\omega$  with positive  $\omega_i$  the  $A$ -contour becomes pinched between them. If this happens, the  $F$ -contour cannot be brought below the real axis. This is the case shown in Figure 2c. The pinching frequency  $\omega^o$  is a branch point of the function  $\alpha(\omega; \beta, R)$  or, equivalently,  $\alpha$  at the pinch point,  $\alpha^o$ , is a saddle point of the function  $\omega(\alpha; \beta, R)$  and at this point  $\partial\omega/\partial\alpha$  is zero. As discussed below, the necessary branch cut originating at  $\omega^o$  in the upper-half  $\omega$ -plane implies that the time-asymptotic response is unbounded for all points in space and the flow is absolutely unstable. In contrast, when no pinching occurs the  $F$ -contour can be lowered below the real axis and the time-asymptotic response is convectively unstable or stable, depending on whether a spatial branch has crossed the real axis or not. The cusp shown in the  $\omega$ -plane in Figure 2c occurs at  $\omega^o$  and is a characteristic feature of a pinch point. In fact, this feature was used by Kupfer et al. [8] to locate absolute instabilities.

As discussed in the previous section, the causality condition invoked by Briggs' method allows a rigorous determination of the direction of energy propagation for spatial waves. With the original inversion contours defined by causality,  $\alpha(\omega_F)$  lies unambiguously in the upper or lower half of the  $\alpha$ -plane and is damped. The half plane in which  $\alpha(\omega_F)$  lies determines whether it gives a response (propagates energy) outward ( $r > r_s$ ) or inward ( $r < r_s$ ) from the source. Lowering of the  $F$ -contour and deformation of the  $A$ -contour may cause a spatial branch to cross the real  $\alpha$ -axis, corresponding to a convectively unstable response either outward or inward from the source depending on which half of the  $\alpha$ -plane it originated in. By careful consideration of the inversion contours, defined by causality arguments, it would be possible to discount the anomalous modes described by Gaster [6] and Salwen and Grosch [9], where these authors had to resort to arguments based on intuition to remove them. No such decision is needed with the procedure described above, which results only in physically acceptable solutions. The real part of the generally complex quantity  $\partial\omega/\partial\alpha$  is often referred to as the (radial) group velocity. This can be misleading, because the path of  $\alpha(\omega_F)$  as the  $F$ -contour is lowered may reverse direction. For example, if  $\alpha(\omega_F)$  originates in the upper-half  $\alpha$ -plane and crosses the real axis as  $\omega_i$  is reduced to zero, this is a convectively unstable response in the region  $r > r_s$ . Here, the sign of the real part of  $\partial\omega/\partial\alpha$  gives the correct information. However, if, after crossing the real  $\alpha$ -axis,  $\alpha(\omega_F)$  starts moving back toward the real axis (remaining in the lower-half  $\alpha$ -plane when  $\omega_i$  is

reduced to zero), which is perfectly possible, locally  $\partial\omega/\partial\alpha$  would have negative real part and imply a damped response in the region  $r < r_s$ , which is incorrect. Examples of this type of behavior are given by Brazier-Smith and Scott [10] and Kupfer et al. [8].

Once the simultaneous deformation of the  $A$ - and  $F$ -contours has taken place, using Briggs' method, the  $\alpha$ -integral

$$\tilde{w} = \frac{1}{2\pi} \int_{A''} \frac{\Phi}{\Delta_0} e^{i(\alpha(r-r_s))} d\alpha, \quad (3.14)$$

which is now integrated along the  $A''$ -contour, can be evaluated by closing the  $A''$ -contour with semicircles, of radius  $\sigma$ , in the upper- and lower-half planes for  $r > r_s$  and  $r < r_s$ , respectively, and using the residue theorem. The semicircular part of the contour in the upper- (denoted by subscript u) and lower-half (denoted by subscript l)  $\alpha$ -plane is represented by  $\Lambda_u$  and  $\Lambda_l$ , respectively. The semicircular contours are deflected around the hyperbolic branch cuts  $\Gamma_{u,l}$  and the imaginary-axis branch cuts  $\Pi_{u,l}$ .

Using the residue theorem for the upper-half plane, contour integration gives

$$\begin{aligned} & \int_{-\sigma}^{+\sigma} \frac{\Phi}{\Delta_0} e^{i\alpha(r-r_s)} d\alpha + \int_{\Lambda_u} \frac{\Phi}{\Delta_0} e^{i\alpha(r-r_s)} d\alpha \\ & + \int_{\Gamma_u} \frac{\Phi}{\Delta_0} e^{i\alpha(r-r_s)} d\alpha + \int_{\Pi_u} \frac{\Phi}{\Delta_0} e^{i\alpha(r-r_s)} d\alpha \\ & = 2\pi i H(r-r_s) \sum_{j=1}^{M_u} \frac{\Phi(z; \alpha_{u_j}(\omega), \omega; \beta, R)}{\frac{\partial \Delta_0(\alpha_{u_j}(\omega), \omega; \beta, R)}{\partial \alpha_{u_j}}} e^{i(\alpha_{u_j}(\omega; \beta, R)(r-r_s))}, \quad (3.15) \end{aligned}$$

for  $r > r_s$ , where the list of variables has been omitted from the left-hand side of the equation,  $H$  is the unit-step function in  $r$  and  $M_u$  is the number of discrete poles  $\alpha_u(\omega; \beta, R)$  of the integrand given by (3.14), caused by the zeros of the dispersion relation, in the upper-half  $\alpha$ -plane. The residues forming the sum on the right-hand side of (3.15) are assumed to be first-order poles; higher-order residues would be obtained by a limiting process of coalescing first-order poles. Similarly, for  $r < r_s$ , the residue

theorem gives

$$\begin{aligned} & \int_{-\sigma}^{+\sigma} \frac{\Phi}{\Delta_0} e^{i\alpha(r-r_s)} d\alpha + \int_{\Lambda_1} \frac{\Phi}{\Delta_0} e^{i\alpha(r-r_s)} d\alpha \\ & + \int_{\Gamma_1} \frac{\Phi}{\Delta_0} e^{i\alpha(r-r_s)} d\alpha + \int_{\Pi_1} \frac{\Phi}{\Delta_0} e^{i\alpha(r-r_s)} d\alpha \\ & = -2\pi i H(r_s - r) \sum_{j=1}^{M_1} \frac{\Phi(z; \alpha_{1_j}(\omega), \omega; \beta, R)}{\frac{\partial \Delta_0(\alpha_{1_j}(\omega), \omega; \beta, R)}{\partial \alpha_{1_j}}} e^{i(\alpha_{1_j}(\omega; \beta, R)(r-r_s))}, \quad (3.16) \end{aligned}$$

where  $M_1$  is the number of discrete poles  $\alpha_1(\omega; \beta, R)$  in the lower-half  $\alpha$ -plane. As  $\sigma \rightarrow \infty$ , the first integrals in Equations (3.15) and (3.16) tend to the  $\alpha$ -inversion (3.14). The integrals over  $\Lambda_{u,1}$  tend to zero as  $\sigma \rightarrow \infty$ . Therefore, the solution of the  $\alpha$ -inversion is given by the residues due to the discrete poles and the continuous spectra, given by the integrations around the branch cuts.

If Briggs' method has resulted in a pinch point between, say, two poles, which by definition must originate in the distinct halves of the  $\alpha$ -plane, the dispersion relation has a double root whose contribution, extracted from the discrete parts of (3.15) and (3.16) is given by

$$\begin{aligned} & ie^{i\beta\theta} H(r - r_s) \frac{\Phi(z; \alpha_u(\omega), \omega; \beta, R)}{\frac{\partial \Delta_0(\alpha_u(\omega), \omega; \beta, R)}{\partial \alpha_u}} e^{i(\alpha_u(\omega; \beta, R)(r-r_s))} \\ & - ie^{i\beta\theta} H(r_s - r) \frac{\Phi(z; \alpha_l(\omega), \omega; \beta, R)}{\frac{\partial \Delta_0(\alpha_l(\omega), \omega; \beta, R)}{\partial \alpha_l}} e^{i(\alpha_l(\omega; \beta, R)(r-r_s))}, \quad (3.17) \end{aligned}$$

which causes a singularity in the remaining  $\omega$ -inversion at  $\omega^o$ . This singularity can be shown by writing the dispersion relation as a Taylor expansion in the vicinity of the branch point, where  $\partial\omega/\partial\alpha = 0$  and therefore  $\partial\Delta_0/\partial\alpha = 0$ ,

$$\begin{aligned} \Delta_0(\alpha, \omega; \beta, R) & \simeq \left[ \frac{\partial \Delta_0}{\partial \omega} \right]_{\alpha^o, \omega^o} (\omega - \omega^o) + \frac{1}{2} \left[ \frac{\partial^2 \Delta_0}{\partial \alpha^2} \right]_{\alpha^o, \omega^o} (\alpha - \alpha^o)^2 \\ & + \left[ \frac{\partial^2 \Delta_0}{\partial \alpha \partial \omega} \right]_{\alpha^o, \omega^o} (\alpha - \alpha^o)(\omega - \omega^o) \\ & + \frac{1}{2} \left[ \frac{\partial^2 \Delta_0}{\partial \omega^2} \right]_{\alpha^o, \omega^o} (\omega - \omega^o)^2. \quad (3.18) \end{aligned}$$

The last two terms of the expansion (3.18) are higher-order terms as  $\omega \rightarrow \omega^o$ , because  $|\alpha - \alpha^o| = O(|\omega - \omega^o|^{1/2})$ . Neglecting these smaller terms, the two coalescing poles occur at

$$\alpha_{u,1} \simeq \alpha^o \pm i \left[ 2 \frac{\partial \Delta_0}{\partial \omega} \right]_{\alpha^o, \omega^o}^{1/2} \left[ \frac{\partial^2 \Delta_0}{\partial \alpha^2} \right]_{\alpha^o, \omega^o}^{-1/2} (\omega - \omega^o)^{1/2}. \quad (3.19)$$

Differentiating (3.18), using  $\partial \omega / \partial \alpha = 0$  at  $\alpha^o$ , and substituting into (3.19) gives, to leading order,

$$\frac{\partial \Delta_0}{\partial \alpha_{u,1}} \simeq \pm i \left[ 2 \frac{\partial \Delta_0}{\partial \omega} \frac{\partial^2 \Delta_0}{\partial \alpha^2} \right]_{\alpha^o, \omega^o}^{1/2} (\omega - \omega^o)^{1/2}. \quad (3.20)$$

The discrete contribution to the  $\omega$ -integrand is then obtained by substituting (3.20) into (3.17) and using the fact that  $H(r_s - r) = 1 - H(r - r_s)$  gives

$$\tilde{w}_D \simeq \frac{\Phi(z; \alpha^o, \omega^o; \beta, R)}{\left[ 2 \frac{\partial \Delta_0}{\partial \omega} \frac{\partial^2 \Delta_0}{\partial \alpha^2} \right]_{\alpha^o, \omega^o}^{1/2}} \frac{e^{i(\alpha^o(r-r_s) + \beta\theta)}}{(\omega - \omega^o)^{1/2}}, \quad (3.21)$$

as  $\alpha_{u,1} \rightarrow \alpha^o$ , for all  $r$ . Clearly, there is a branch cut in the  $\omega$ -plane due to the square root singularity of (3.21) at  $\omega^o$ , which can be taken downward from the branch point at  $\omega^o$ . This singularity imposes a limit on the region of analyticity in the  $\omega$ -plane.

If, say, two poles that both originate in the upper-half  $\alpha$ -plane or both in the lower-half  $\alpha$ -plane coalesce, their residue contributions are of the same type; i.e., both have the form of either the first or the second term of Equation (3.17). These cancel in the limit  $\alpha \rightarrow \alpha^o$ . This is to be expected, since a second-order pole that lies inside a closed contour (in this case, the contour is not constrained to pass between the merging poles) makes a finite contribution to the contour integral (3.15) or (3.16) when using the residue theorem. Such a case ultimately behaves according to linear theory; however, there is a short period of algebraic growth, which may be important if the second-order pole is near neutral. This idea is not pursued here but has been studied by Benney and Gustavsson [11], Koch [12], and Henningson et al. [13].

Assuming that a single pinch point in the upper-half  $\omega$ -plane exists, the major time-asymptotic contribution to  $w(z; r, \theta, t)$  from the discrete spectrum  $\tilde{w}_D$ , comes from the branch pole at  $\omega^o$ . (If there is more than one pinch point, the one lying highest in the  $\omega$ -plane is dominant.) In the limit  $t \rightarrow \infty$ , the asymptotic response of  $w_D(z; r, \theta, t)$  can be represented, for all  $r$ ,

by

$$\begin{aligned}
 w_D(z; r, \theta, t) &\sim \frac{1}{2\pi} \frac{\Phi(z; \alpha^o, \omega^o; \beta, R)}{\left[2(\partial\Delta_0/\partial\omega)(\partial^2\Delta_0/\partial\alpha^2)\right]_{\alpha^o, \omega^o}^{1/2}} e^{i(\alpha^o(r-r_s)+\beta\theta)} \\
 &\quad \times \int_{F''} \frac{e^{-i\omega t}}{(\omega - \omega^o)^{1/2}} d\omega \\
 &\sim \frac{\Phi(z; \alpha^o, \omega^o; \beta, R)}{\left[2\pi i t(\partial\Delta_0/\partial\omega)(\partial^2\Delta_0/\partial\alpha^2)\right]_{\alpha^o, \omega^o}^{1/2}} e^{i(\alpha^o(r-r_s)+\beta\theta - \omega^o t)},
 \end{aligned} \tag{3.22}$$

where  $F''$  is the deformed contour shown in Figure 3. The integral in Equation (3.22) can be evaluated using the substitution  $\omega' = (\omega - \omega^o)^{1/2} t^{1/2}$ . Since  $\omega_i^o$  has been assumed to be positive, the response given by Equation (3.22) grows in time and indicates absolute instability. In general,  $\alpha^o$  is complex and so the discrete response will have an exponential envelope in space. Equation (3.22) is valid for all finite  $r$  and is continuous through  $r_s$  and the absolute instability represents a normal mode of the flow that corresponds to the amplitude build-up of an oscillator. This process can be initiated by noise or any other excitation and leads to a state determined by nonlinear effects.

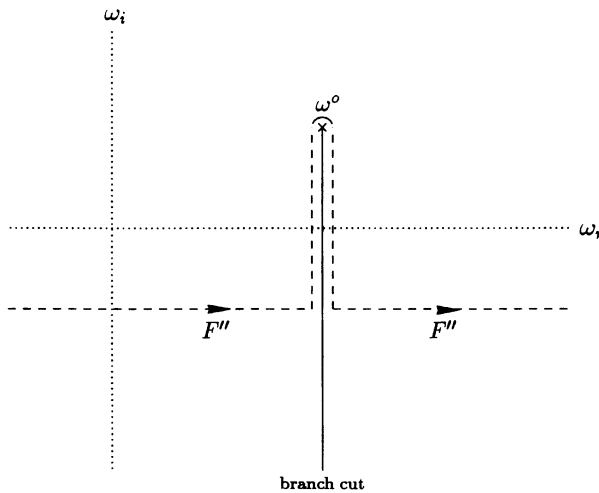


Figure 3. A sketch of the deformed integration contour (---) in the  $\omega$ -plane;  $\omega^o$  is marked by  $\times$  and the branch cut is marked by —.

Of course, the response (3.22) would be truly valid for all  $r$  only if the flow were parallel. In practice, the analysis is applied at a range of Reynolds numbers, or radii, where the flow is assumed to be locally parallel. With this assumption, if the flow changes from a convectively unstable to an absolutely unstable regime at a certain Reynolds number, then the bounded response becomes unbounded at the corresponding radius. Also, it should be noted that Equation (3.22) is not valid for large  $r$ , i.e., near the front of the wave packet, because  $r$  was kept constant as  $t \rightarrow \infty$ . This problem is overcome by letting  $r$  and  $t$  tend to infinity, while  $r/t$  is kept constant. This is the approach taken in the method of steepest descent. However, the method of steepest descent has problems of its own, which are discussed in Section 3.1.2.

If there are no pinch points in the upper-half  $\omega$ -plane (or none at all) the  $F''$ -contour can lie completely below the real axis, so the entire upper-half  $\omega$ -plane is analytic and the time-asymptotic response of the discrete spectrum tends to zero as  $t \rightarrow \infty$ . Thus, to summarize, Briggs' criterion requires a branch-point singularity between two or more spatial branches of the dispersion relation, of which at least two must lie in distinct halves of the complex  $\alpha$ -plane, when  $\omega_i$  is sufficiently large and positive; i.e., at least two must give responses in the distinct physical regions  $r > r_s$  and  $r < r_s$ .

As discussed above, the response of the discrete spectrum can distinguish between convectively and absolutely unstable time-asymptotic responses. However, the structure of the response through the boundary layer close to the source of the initial perturbation depends on the continuous spectra. Because the branch cuts in the upper-half (lower-half)  $\alpha$ -plane do not cross into the lower-half (upper-half)  $\alpha$ -plane, even when the  $F''$ -contour is constrained to remain in the upper-half  $\omega$ -plane due to a pinch point, the spatial response due to the branch cuts at fixed  $t$  tends to zero as  $|r - r_s| \rightarrow \infty$ , which is why the continuous spectra for other boundary-layer flows are often referred to as the near (or local) field. However, if there is a pinch point in the upper-half  $\omega$ -plane, the  $F''$ -contour must pass above  $\omega^o$  (see Figure 3), and therefore the time-asymptotic response to the continuous spectra will be growing in time. It should be emphasized that the continuous spectra only cause temporal growth if the discrete spectrum is also temporally growing (absolutely unstable); therefore the response to the discrete spectrum is enough to indicate the nature of the instability.

**3.1.2. The method of steepest descent.** The integrals given by (3.11) give the exact solution for the axial perturbation velocity  $w$ , when the boundary-layer flow is impulsively disturbed in the way described by (2.18). The solution can be evaluated by direct numerical integration, or, alternatively, time-asymptotic methods of evaluation, in which only dominant terms are considered, can be used. In Section 3.1.1, the integrals given by (3.11) were



estimated using Briggs' method, in which the  $\alpha$ -inversion is performed first, followed by the time-asymptotic solution to the  $\omega$ -inversion. However, because  $r$  is kept fixed as  $t \rightarrow \infty$ , the solution of the discrete spectrum is not valid near the front of the wave packet. Nevertheless, this method elegantly distinguishes between convectively and absolutely unstable flow regimes. In this section, the method of steepest descent (or saddle-point method), in which  $(r - r_s)/t$  is kept constant as  $t \rightarrow \infty$ , is used to give time-asymptotic approximations to impulsive point forcing. The method of steepest descent is a widely used way of examining the time-asymptotic behavior of disturbances in various flows, e.g., [14–17] for flat-plate boundary layers, [18] for free shear layers, and [19] for stationary disturbances in the rotating-disk boundary layer. In common with [20], no attempt is made to represent the full mathematical solution to the initial boundary-value problem; i.e., the continuous spectra will be neglected. Then the dominant contribution is given by saddle points of the complex phase function enabling wave packets to be calculated.

Previously, the method of steepest descent has been used to complete the  $\alpha$ -inversion, after the  $\omega$ -inversion has been performed, which is the opposite order to that used in Briggs' method but which is equally valid. However, it is often stated (e.g., [21]) that to distinguish between convective and absolute instability using the method of steepest descent, it is necessary to calculate only the solution for  $(r - r_s)/t = 0$ . If it is temporally growing the flow is absolutely unstable. It is shown in the following section that for the particular ray (in the space–time domain), where  $(r - r_s)/t = 0$ , the saddle point of the phase function occurs where  $\partial\omega/\partial\alpha = 0$  and therefore coincides with a saddle point of the dispersion relation. As discussed in Section 3.1.1, a saddle point of the dispersion relation only dominates the time-asymptotic solution if it is of the pinch type, and not if the two coalescing branches of the dispersion relation give responses in the same direction away from the source. However, if the method of steepest descent is used blindly, which seems to be the case in the majority of the literature (e.g., [14–17, 19, 21]), no distinction is made between different types of saddle points and incorrect conclusions about the instability characteristics of the flow can be drawn. Examples are given showing that it is not sufficient simply to locate the various saddle points of the complex phase function without determining the global topography of the phase function, from which the saddle points that are relevant to the  $\omega$ -inversion can be isolated. It is shown that the method of steepest descent can be used to distinguish between convective and absolute instability and to illustrate the time-asymptotic form of the wave packet, but only if the inversion contours are chosen correctly.

Here, to calculate the time-asymptotic response to (3.11), with the  $F$ - and  $A$ -contours defined by causality and convergence arguments (as described in Section 3.1), the  $\omega$ -integral is performed first by closing the  $F$ -contour with

semicircles at infinity and using the residue theorem. The branch-cut contributions are omitted, leaving the discrete spectrum due to the zeros of the dispersion relation, which must all lie below the  $F$ -contour, given by

$$w(z; r, \theta, t) = \frac{H(t)i^{i\beta\theta}}{2\pi i} \int \sum_{j=1}^M \Theta_j(z; \alpha) e^{\psi_j(\alpha)t} d\alpha, \quad (3.23)$$

where

$$\Theta_j(z; \alpha) = \frac{\Phi(z; \alpha, \omega_j(\alpha); \beta, R)}{\partial \Delta_o(\alpha, \omega_j(\alpha); \beta, R) / \partial \omega_j}, \quad (3.24)$$

and

$$\psi_j(\alpha) = i \left( \frac{\alpha(r - r_s)}{t} - \omega_j(\alpha) \right). \quad (3.25)$$

Here,  $\psi_j$  is the complex phase function,  $M$  is the number of discrete first-order poles  $\omega_j(\alpha)$  of the  $\omega$ -integrand, and  $H(t)$  is the unit-step function in time. In general, the function  $\Theta_j(z; \alpha)$  has branch-pole singularities at branch points of  $\omega(\alpha)$ , where  $\partial \Delta_o / \partial \omega = 0$  and  $\partial \omega / \partial \alpha = \infty$ , and these arise when poles coalesce. However, the sum over all  $j$  does not have any singularities; the summation  $\sum_{j=1}^M \Theta_j(z; \alpha)$  is an entire function. This must be so, because the branch points of  $\omega(\alpha)$  are just double roots of  $\omega$  for some  $\alpha$  and both roots are always included in the residue evaluation. The two terms that individually have a singularity therefore cancel. Clearly, it is not possible for a double root of  $\omega$  to pinch the  $F$ -contour because there are no discrete poles above the  $F$ -contour from causality arguments.

*General formulation:* The method of steepest descent can be applied to nonconservative wave systems with complex  $\omega$  to evaluate the remaining  $\alpha$ -integral at large time. The best approximation to the  $\alpha$ -inversion is given by choosing a path where large values of  $\psi_{jr}(\alpha)$  are concentrated in as short a length as possible and where  $\psi_j$  is stationary. When  $\partial^2 \psi_j / \partial \alpha^2 \neq 0$ , it is easy to show (using the Cauchy–Riemann equations) that, for given  $(r - r_s)/t$  and  $(R$  and  $\beta)$ , there are no maxima or minima of either  $\psi_{jr}(\alpha)$  or  $\psi_{ji}(\alpha)$ ; therefore all stationary points of  $\psi_j(\alpha)$ , where  $\partial \psi_j / \partial \alpha = 0$ , are saddle points. So, if the end points of the integration are separated by, say, a single saddle point of  $\psi_j(\alpha)$ , the original  $A$ -contour (along the real axis) is deformed onto a steepest-descent path that passes through the saddle point  $\alpha^*$ , where  $\omega_j(\alpha^*) = \omega_j^*$  and  $(\partial \psi_j / \partial \alpha)_{\alpha^*, \omega_j^*} = 0$ . A steepest-descent path lies along a line where  $\psi_{jr}(\alpha)$  decreases most rapidly, namely orthogonal to the lines of constant  $\psi_{jr}(\alpha)$ , and is therefore (from the Cauchy–Riemann

equations) given by a line of constant  $\psi_{ji}(\alpha)$  through the saddle point. In general, the limits of the integral do not lie on the steepest-descent path, but they can be joined to it within valleys of  $\psi_{jr}(\alpha)$ , i.e., within regions where  $\psi_{jr}(\alpha) < \psi_{jr}(\alpha^*)$ .

As  $t \rightarrow \infty$  with fixed  $(r - r_s)/t$ , integration along the steepest-descent path is dominated by the contribution given by the saddle point of  $\psi_j(\alpha)$ . At these saddle points

$$\left[ \frac{\partial \omega}{\partial \alpha} \right]_{\alpha^*, \omega_j^*} = \frac{r - r_s}{t}, \quad (3.26)$$

which is real and therefore

$$\left[ \frac{\partial \omega_r}{\partial \alpha_r} \right]_{\alpha^*, \omega_j^*} = \frac{r - r_s}{t}, \quad \left[ \frac{\partial \omega_i}{\partial \alpha_r} \right]_{\alpha^*, \omega_j^*} = 0. \quad (3.27)$$

Assuming that there is a single saddle point of  $\psi_j$  through which the integration contour can be made to pass for each value of  $j$  and provided  $(\partial^2 \omega / \partial \alpha^2)_{\alpha^*, \omega_j^*}$  is nowhere zero, following any standard mathematics text book (e.g., [22]), the time-asymptotic impulse response to (3.23) reduces to

$$w(z; r, \theta, t) \sim -iH(t)e^{i\beta\theta} \sum_{j=1}^M \frac{\Theta(z; \alpha^*)e^{i(\alpha^*(r-r_s)-\omega_j^*t)}}{[2\pi it(\partial^2 \omega / \partial \alpha^2)]_{\alpha^*, \omega_j^*}^{1/2}}. \quad (3.28)$$

The validity of the first of these assumptions is discussed below. In practice, for the time-asymptotic response, the summation over  $M$  is limited to the number of unstable modes, namely  $M=2$  for the rotating-disk boundary layer.

As  $(r - r_s)/t$  varies with  $\beta$  constant, the saddle point traces a path in the  $\alpha$ -plane, each point being related to a ray in the physical  $(r, t)$ -space. Along each  $[(r - r_s)/t]$ -ray the response is dominated by the exponential term of Equation (3.28) and has the form of a traveling wave with constant complex values of radial wavenumber  $\alpha^*$  and frequency  $\omega_j^*$ . The temporal growth rate, along a ray, is

$$\psi_{jr}^* \equiv \psi_{jr}(\alpha^*) = \left( \omega_{ji}^* - \frac{\alpha_i^*(r - r_s)}{t} \right). \quad (3.29)$$

Following the response along any given  $[(r - r_s)/t]$ -ray corresponds to a moving observation position traveling at  $[\partial \omega / \partial \alpha]_{\alpha^*, \omega_j^*}$  [see (3.27)], and if

$\psi_{jr}^*$  is positive the disturbance grows in time in that reference frame. If  $\psi_{jr}^*$  is negative, the waves decay in amplitude as they travel and the flow returns to its undisturbed state.

*Saddle points of the complex phase function:* In this section, the subscripts  $j$ , which have been used above to distinguish between the two temporal modes given by real  $\alpha$ , are omitted. For complex  $\alpha$  on the steepest-descent path, continuation of the two temporal modes forms two Riemann sheets of  $\omega(\alpha)$ , which are joined, in general, at a complex value of  $\alpha$  that is a branch point of  $\omega(\alpha)$  and where  $\partial\omega/\partial\alpha = \infty$ . The branch cut that necessarily comes from the branch point can be arbitrarily chosen. Because of this arbitrary choice, the distinction between the two modes for complex  $\alpha$  is blurred. Nonetheless, both modes are still considered.

The temporal branches of the dispersion relation given by real values of  $\alpha$  can be used to identify certain saddle points of  $\psi(\alpha)$ . In Figure 4, two temporal branches are shown for  $R = 460$  and  $\beta = 20$ , where only one of the branches is amplified (the one with  $\omega_i > 0$ ). The damped  $\omega_i$ -curve has no turning points, but the amplified  $\omega_i$ -curve has two maxima and one minimum. At such turning points,  $\partial\omega_i/\partial\alpha_r = 0$  and  $\partial\omega_r/\partial\alpha_r$  has some real value, which are the requirements for a saddle point of the phase function, given by (3.27), at  $(r - r_s)/t = \partial\omega_r/\partial\alpha_r$ . Furthermore, by differentiating the temporal growth rate  $\psi_r^*$  with respect to  $(r - r_s)/t$ , it is easy to show that maxima and minima of  $\psi_r^*$  occur when  $\alpha_i = 0$  and are given by the maxima and minima, respectively, of the  $\omega_i$ -branches given by real  $\alpha$ . Therefore, the turning points of  $\omega_i$  on temporal branch 1 in Figure 4a correspond to turning points of  $\psi_r^*$  with respect to  $(r - r_s)/t$ .

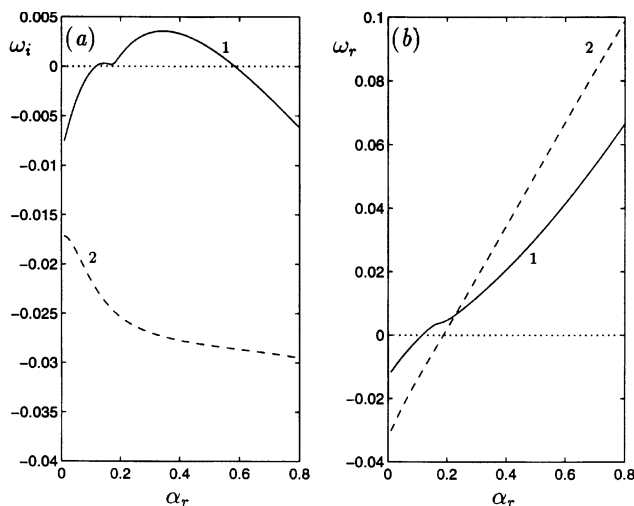


Figure 4. Temporal branches 1 and 2 ( $\alpha_i = 0$ ) for  $R = 460$  and  $\beta = 20$ : (a)  $\omega_i$  against  $\alpha_r$ , (b)  $\omega_r$  against  $\alpha_r$ .

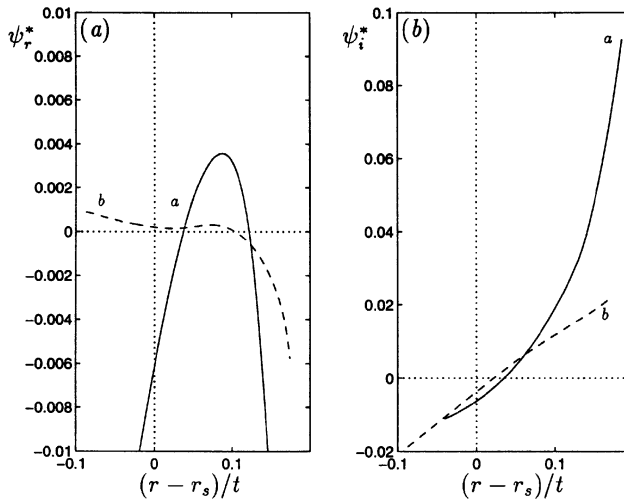


Figure 5. Saddle-point trajectories for  $R = 460$  and  $\beta = 20$ : (a)  $\psi_r^*$  against  $(r - r_s)/t$ , (b)  $\psi_i^*$  against  $(r - r_s)/t$ . At  $(r - r_s)/t = 0$ ,  $\psi^*$  on trajectory  $a$  corresponds to a branch point between branches 1 and 3, and  $\psi^*$  on trajectory  $b$  is a branch point between 1 and 2.

Figure 5 shows  $\psi_r^*$  and  $\psi_i^*$  plotted against  $(r - r_s)/t$ . The large branch 1 maximum in  $\omega_i$  gives values of  $\alpha$  and  $\omega$  for a saddle point at  $(r - r_s)/t \approx 0.0875$  (where trajectory  $a$  in Figure 5a has a maximum), the smaller branch 1 maximum corresponds to a saddle point at  $(r - r_s)/t \approx 0.0720$  (where trajectory  $b$  in Figure 5a has a maximum) and the branch 1 minimum corresponds to a saddle point at  $(r - r_s)/t \approx 0.0235$  (where trajectory  $b$  in Figure 5a has a minimum). From these starting points, the remainder of trajectories  $a$  and  $b$  can be calculated.

As mentioned above, it is often stated that to distinguish between convectively and absolutely unstable time-asymptotic responses, it is necessary only to look at the behavior along the ray of zero  $(r - r_s)/t$ , i.e., at the fixed spatial location  $r = r_s$  as  $t \rightarrow \infty$ . From the saddle-point condition (3.27), it is clear that along this ray  $\partial\omega/\partial\alpha$  is identically zero and that the phase function reduces to  $-i\omega^*$ . Therefore,  $\omega^*$  on this ray is a branch point of  $\alpha(\omega)$ ; equivalently,  $\alpha^*$  is a saddle point of  $\omega(\alpha)$ , as well as  $\psi(\alpha)$ . Thus, the saddle points of the phase function for  $(r - r_s)/t = 0$  are also saddle points of the dispersion relation. In Figure 5,  $\omega^*$  at  $(r - r_s)/t = 0$  on trajectories  $a$  and  $b$  are branch points between spatial branches 1 and 3 and spatial branches 1 and 2, respectively.<sup>1</sup> Application of Briggs' method shows that the

<sup>1</sup> Spatial branches 1 and 3 are inviscidly unstable and spatial branch 2 is viscously unstable; see [2]. Further, branches 1 and 2 apply downstream of the source and can be convectively unstable, whereas branch 3 applies upstream of the source but is always convectively stable. The temporal branches labeled 1 and 2 in Figure 4 have the same neutral points (points lying on the neutral-stability curve for convective instability, where  $\alpha_i = \omega_i = 0$ ) as spatial branches 1 and 2; spatial branch 3 has no neutral points because it is always convectively stable.

latter branch point is the type that does not cause absolute instability, because branches 1 and 2 both originate in the upper-half  $\alpha$ -plane of large positive  $\omega_i$ , whereas branches 1 and 3 originate in distinct halves of the  $\alpha$ -plane and  $\omega^*$  is a pinch point of  $\alpha(\omega)$ , which can give absolute instability if  $\omega_i^*$  is positive.

For the values of  $R$  and  $\beta$  chosen for Figure 5,  $\omega_i^*$  at the pinch point between branches 1 and 3, and also  $\psi_r^*$  at  $(r - r_s)/t = 0$ , is negative and therefore the flow is absolutely stable (the critical Reynolds number for the onset of absolute instability has been shown in [2] to be  $R \approx 510$ ). Trajectory *a* saddle points, continuing from the pinch point between branches 1 and 3, have positive  $\psi_r^*$  for a range of  $(r - r_s)/t$  between about 0.037 and 0.122. These bounding rays define a wedge of convective instability. The value of  $\psi_r^*$  for  $(r - r_s)/t = 0$  on trajectory *b* is positive, which seems to suggest that the branch point between branches 1 and 2 gives an absolutely unstable response, which is known to be false from the earlier discussion of Briggs' method. Moreover,  $\psi_r^*$  becomes increasingly positive as  $(r - r_s)/t$  takes more negative values, which implies an ever growing response inward from the source. Clearly, this behavior contradicts the results obtained from the inversions performed using Briggs' method, which give only a growing response inward from the source if there is a pinch point between branches 1 and 3 with positive  $\omega_i$ , and even then the response is damped for  $r$  sufficiently less than  $r_s$  at fixed time.

The anomalous behavior of trajectory *b* emphasizes the fact that it is not enough to locate the various saddle points of  $\psi(\alpha)$ ; the saddle points that are relevant to the  $\alpha$ -inversion must be determined from the global topography of the phase function, which is described below. Figures 6a and 6b show contour plots of the real (solid lines) and imaginary (dotted lines) parts of

$$\Psi(\alpha) \equiv i\psi(\alpha) = \left( \omega(\alpha) - \frac{\alpha(r - r_s)}{t} \right) \quad (3.30)$$

in the complex  $\alpha$ -plane for  $R = 460$ ,  $\beta = 20$ , and  $(r - r_s)/t = 0$ ; similarly Figures 6c and 6d show contour plots of the real and imaginary parts of  $\Psi(\alpha)$  for  $R = 460$ ,  $\beta = 20$ , and  $(r - r_s)/t = 0.03$ . When  $(r - r_s)/t = 0$ ,  $\Psi(\alpha)$  is equal to  $\omega(\alpha)$ , which explains why the factor of  $i$  has been introduced in (3.30). This equivalence makes comparisons between results from the Briggs' method inversions and those from the steepest-descent method easier. The relationship between  $\Psi(\alpha)$  and  $\psi(\alpha)$  is a simple rotation through  $\pi/2$ ; therefore a steepest-descent path has constant  $\Psi_r(\alpha)$  and passes through valleys of  $\Psi_i(\alpha)$ , having its highest value of  $\Psi_i(\alpha)$  at the saddle point  $\alpha^*$ . Conditions for a saddle point of  $\Psi(\alpha)$  are the same as those for a saddle point of  $\psi(\alpha)$ , given by (3.27).

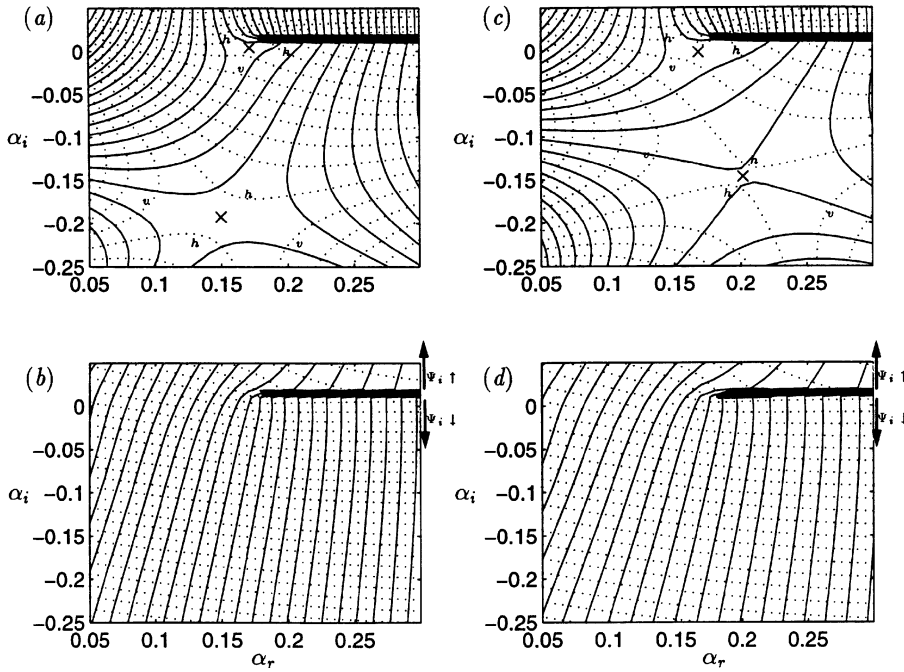


Figure 6. Contours of the  $\Psi_r(\alpha)$  (—) and  $\Psi_i(\alpha)$  (···) plotted in the  $\alpha$ -plane for  $R = 460$  and  $\beta = 20$ : (a, b)  $(r - r_s)/t = 0$ , (c, d)  $(r - r_s)/t = 0.03$ . Saddle points of  $\Psi(\alpha)$  are marked by  $\times$ , v and h indicate the valleys and hills of  $\Psi_i(\alpha)$  around the saddle points, respectively, and branch cuts that separate the two Riemann sheets are represented by thick horizontal lines. The spacing of the contours in (b) and (d) is double that in (a) and (c).

For each value of  $(r - r_s)/t$ , there are two Riemann sheets of  $\Psi(\alpha)$ , examples of which are shown separated by an arbitrarily chosen horizontal branch cut in the upper right-hand corner of the plots in Figure 6. The branch cuts terminate at values of  $\alpha$  that are branch points of  $\Psi(\alpha)$ , i.e., points where  $\partial\Psi/\partial\alpha = \infty$ . The two Riemann sheets are a consequence of the temporal branches 1 and 2 shown in Figure 4. In Figures 6a and 6b, where  $(r - r_s)/t = 0$ , the Riemann sheets are direct continuations of the purely temporal modes into regions of nonzero  $\alpha_i$ . For  $(r - r_s)/t = 0.03$  (and any other value of  $(r - r_s)/t$ ), in Figures 6c and 6d, the Riemann sheets are derived from the sheets of the dispersion relation via Equation (3.30). Saddle points of  $\Psi(\alpha)$  are clearly visible in Figures 6a and 6c and the valleys and hills of  $\Psi_i(\alpha)$  that surround the saddle points are marked (where possible) with a v and h, respectively. The saddle points in the lower-half  $\alpha$ -plane lie on trajectory *a* in Figure 5; therefore  $\omega^*$  at the lower saddle point in Figure 6a is a pinch point between branches 1 and 3 of the dispersion relation. The higher saddle points lie on trajectory *b*; therefore, when  $(r - r_s)/t = 0$ ,  $\omega^*$  is a branch point between branches 1 and 2 of the dispersion relation.

In general, if there are two saddle points, and it is possible to traverse from one steepest-descent path to the other within valleys of  $\Psi_i(\alpha)$ , then both saddle points contribute to the integral, although in general one usually dominates. Thus, having isolated two saddle points for any particular combination of  $R$ ,  $\beta$ , and  $(r - r_s)/t$ , it remains to establish whether the original  $A$ -contour, which lies along the real  $\alpha$ -axis, can be deformed to pass through them. In Figure 7 the steepest-descent path that passes through a trajectory  $a$  saddle point is mapped from the complex  $\Psi$ -plane to the  $\alpha$ -plane for  $R = 460$  and  $\beta = 20$ . Figures 7a and 7c are for  $(r - r_s)/t = 0$  and Figures 7b and 7d are for  $(r - r_s)/t = 0.1$ . The solid vertical lines marked by  $S$  are steepest-descent paths in the  $\Psi$ -plane, which by definition have constant  $\Psi_r$  and have a maximum value of  $\Psi_i$  at the branch point that maps to the saddle point in the  $\alpha$ -plane (both marked by  $\circ$ ). The steepest-descent paths  $S$  map to  $\alpha(\Psi_S)$ , which pass through the saddle point in the  $\alpha$ -plane. Vertical continuation of  $S$  would map to steepest-ascent paths, which would be perpendicular to the steepest-descent paths at the saddle points. Each value of  $\Psi$  on the steepest-descent path (apart from the branch point itself)

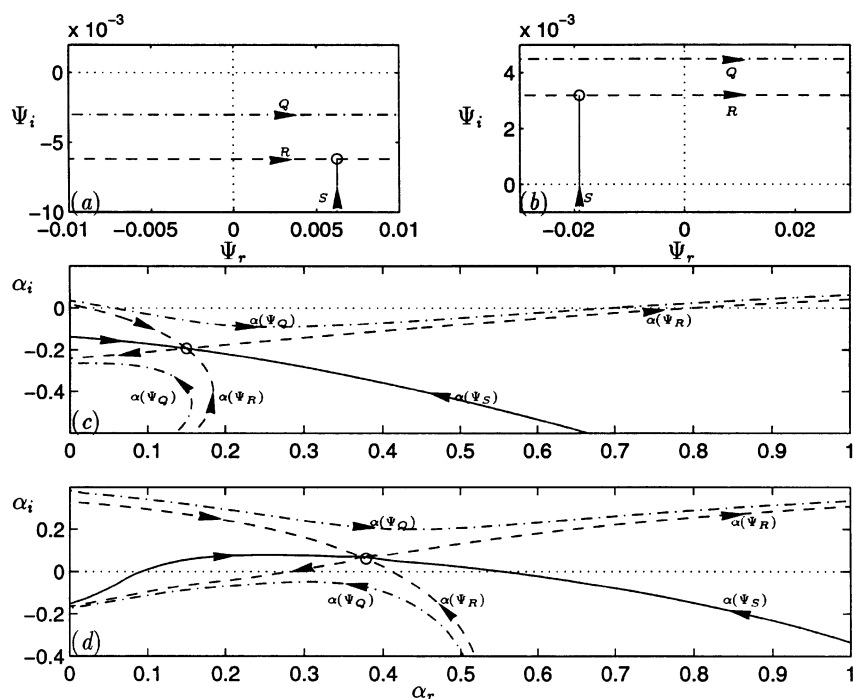


Figure 7. Mapping of steepest-descent paths ( $S$ ) from the  $\Psi$  to the  $\alpha$ -plane ( $\alpha(\Psi_S)$ ) through trajectory  $a$  saddle points ( $\circ$ ), for  $R = 460$  and  $\beta = 20$ : (a, b)  $(r - r_s)/t = 0$ , (b, d)  $(r - r_s)/t = 0.1$ . Saddle-point heights and the high ground relative to the saddle points are marked by  $\alpha(\Psi_R)$  and  $\alpha(\Psi_Q)$ , respectively, the arrows indicate the direction of increasing  $\Psi_r$ .



maps to two values of  $\alpha$ : one on each side of the saddle point. The horizontal dashed lines in the  $\Psi$ -plane marked by  $R$ , when mapped to the  $\alpha$ -plane, give the height of the saddle points and therefore bound the valleys of  $\Psi_i$ , through which the steepest-descent paths must pass. Each value of  $\Psi$  on  $R$  maps to two values of  $\alpha(\Psi_R)$ : one on each side of the saddle point. Similarly, the horizontal lines in the  $\Psi$ -plane marked by  $Q$  map to  $\alpha(\Psi_Q)$ , which lie on the high ground relative to the saddle point. Note that lines of  $\alpha(\Psi)$  in Figure 7c are equally lines of  $\alpha(\omega)$  and are therefore equivalent to particular contour levels of constant  $\psi_r$  and  $\psi_i$  in Figure 6. The results for  $(r - r_s)/t = 0$  and  $(r - r_s)/t = 0.1$  are qualitatively similar, as they are for all trajectory  $a$  saddle points, and the values of  $\Psi$  at the branch points are pinch points of  $\alpha(\Psi)$ . Therefore, in this case the steepest-descent method gives contributions to the physical solution for rays covering the entire wave packet.

It can be shown that close to, and on either side of, a saddle point in the  $\alpha$ -plane, the steepest-descent path lies at angles of

$$\pm \frac{\pi}{2} - \frac{\eta}{2}, \quad (3.31)$$

where

$$\eta = \tan^{-1} \left( - \left[ \frac{\partial^2 \omega_r}{\partial \alpha_r^2} \right]_{\alpha^*, \omega^*} \left[ \frac{\partial^2 \omega_i}{\partial \alpha_r^2} \right]_{\alpha^*, \omega^*}^{-1} \right). \quad (3.32)$$

Moreover, the valleys are given locally by angles  $\vartheta$  lying in the ranges

$$\frac{\pi}{4} - \frac{\eta}{2} < \vartheta < \frac{3\pi}{4} - \frac{\eta}{2}, \quad (3.33)$$

$$-\frac{3\pi}{4} - \frac{\eta}{2} < \vartheta < -\frac{\pi}{4} - \frac{\eta}{2}. \quad (3.34)$$

For example, in Figure 7c,  $\eta \approx -128.6^\circ$  so close to the saddle point the steepest-descent path lies at about  $154.3^\circ$  and  $-25.7^\circ$ , and the valleys lie between  $109.3^\circ$  and  $199.3^\circ$  and between  $-70.7^\circ$  and  $19.3^\circ$ .

As mentioned above, for  $(r - r_s)/t = 0$  the  $\Psi$ -plane is equivalent to the  $\omega$ -plane. In fact,  $\alpha(\Psi_R)$  in Figure 7c is equivalent to  $\alpha(\omega_{F''})$  sketched in Figure 2c and shown in Figure 9b of [2] (for different  $R$  and  $\beta$ ), in both of which there is a pinch point between coalescing spatial branches that originate in distinct halves of the  $\alpha$ -plane for large  $\omega_i$ , i.e., branches 1 and 3. Moreover, taking the integration contour along the steepest-descent path  $\alpha(\omega_s) \equiv \alpha(\Psi_s)$  can be shown, by a change of variable, to be equivalent to the final  $\omega$ -inversion using Briggs' method when there is a pinch point. Thus,

the general steepest-descent solution, given by (3.28), at  $r = r_s$  is, in fact, exactly the same solution as that derived from Briggs' method, given by (3.22).

For  $(r - r_s)/t = 0$ , where  $\partial\Delta_0/\partial\alpha = \partial\omega/\partial\alpha = 0$  at the saddle point, the argument proceeds as follows. The steepest-descent inversion

$$I = \frac{e^{i\beta\theta}}{2\pi i} \int_{\alpha(\omega_s)} \left( \frac{\Phi(z; \alpha, \omega(\alpha); \beta, R)}{\partial\Delta_0(\alpha, \omega(\alpha); \beta, R)/\partial\omega} \right) e^{-i\omega(\alpha)t} d\alpha, \quad (3.35)$$

which has been extracted from Equations (3.23)–(3.25), is considered with the assumption that  $\partial\Delta_0/\partial\omega \neq 0$  near the steepest-descent path, implying that the two sheets of  $\Psi(\alpha) \equiv \omega(\alpha)$  can be dealt with separately. By changing the integration variable to  $\omega$ , the integral can be written as

$$I = \frac{e^{i\beta\theta}}{2\pi i} \int_{\omega_s} \left( \frac{\Phi(z; \alpha, \omega(\alpha); \beta, R)}{\partial\Delta_0(\alpha, \omega(\alpha); \beta, R)/\partial\omega} \frac{\partial\alpha}{\partial\omega} \right) e^{-i\omega t} d\omega, \quad (3.36)$$

where the integration contour is the mapping of the steepest-descent path in the  $\alpha$ -plane to the  $\omega$ -plane, i.e.,  $\omega_s \equiv \Psi_s$  (see Figure 7a). Since a value of  $\alpha$  on either side of the saddle point map to the same  $\omega$ , the values of  $\omega$  on the integration contour  $\omega_s$  can be imagined approaching the branch point from underneath and then reversing direction at the branch point, moving away vertically downward, thus collecting the second  $\omega_s$  from a value of  $\alpha$  on the other side of the saddle point. The solution of (3.36) requires the inverse relation  $\alpha(\omega)$ , enabling the bracketed term in the integral to be expressed as a function of  $\omega$ . The inversion theorem states that the inverse function is well defined, within the region of interest, provided the function itself is analytic in  $\alpha$  and the inverse function is analytic and single valued or capable of being made so by introducing appropriate branch cuts. The assumption that there are no zeros of  $\partial\Delta_0/\partial\omega$  in the region of interest implies that no  $\alpha$  lying within that region is a branch point of  $\omega(\alpha)$  and, in general, that the function  $\omega(\alpha)$  is analytic.

The dominant contribution to (3.36) is then given by the region close to  $\alpha^*$ . Thus, using (3.20), the steepest-descent inversion, with a branch cut extending vertically downward from  $\omega^*$ , (3.36) becomes

$$I \sim \frac{e^{i\beta\theta}}{2\pi} \frac{\Phi(z; \alpha^*, \omega^*; \beta, R)}{[(2\partial\Delta_0/\partial\omega)(\partial^2\Delta_0/\partial\alpha^2)]_{\alpha^*, \omega^*}^{1/2}} \int_{\omega_s} \frac{e^{-i\omega t}}{(\omega - \omega^*)^{1/2}} d\omega, \quad (3.37)$$

such that  $\omega_s$  passes up one side of the branch cut, around the branch point, and down the other side. Equation (3.37) is the same as Equation (3.22) with

$r = r_s$ ,  $F'' \equiv \omega_s$  (the vertical branch cut part of  $F''$  [see Figure 3]),  $\alpha^\circ \equiv \alpha^*$ , and  $\omega^\circ \equiv \omega^*$ , which gives the  $\omega$ -inversion of the discrete spectrum from Briggs' method when there is a pinch point. Because  $\partial\omega/\partial\alpha = 0$  at  $\alpha^*$ ,

$$\left[ \frac{\partial^2 \omega}{\partial \alpha^2} \right]_{\alpha^*, \omega^*} = - \left[ \frac{\partial^2 \Delta_0}{\partial \alpha^2} \right]_{\alpha^*, \omega^*} \left[ \frac{\partial \Delta_0}{\partial \omega} \right]_{\alpha^*, \omega^*}^{-1}, \quad (3.38)$$

and therefore the result of (3.37), which is given by (3.22) for  $r = r_s$ , is the same as the general steepest-descent result for a  $j$ th component and  $r = r_s$ , given by (3.28). This equivalence between the two methods is to be expected, because the steepest-descent method, from which only the standard result has been given here, involves an explicit change of variable from  $\alpha$  to a variable that is real on the steepest-descent path that can be shown to be a simple function of  $\omega$  for the case of  $(r - r_s)/t = 0$ .

Clearly, the  $A$ -contour can be deformed onto steepest-descent paths through trajectory  $a$  saddle points, which correspond to pinch points between two branches of  $\alpha(\Psi_R)$  that originate in distinct halves of the  $\alpha$ -plane for large positive  $\Psi_i$ ; it remains only to check that end points of the integration lie in valleys of  $\Psi_i$  and for the examples shown in Figure 7 this is indeed the case. However, the trajectory  $b$  saddle points provide examples where this is not the case. Figure 8 shows how the steepest-descent path that passes through a trajectory  $b$  saddle point is mapped from the  $\Psi$ -plane to

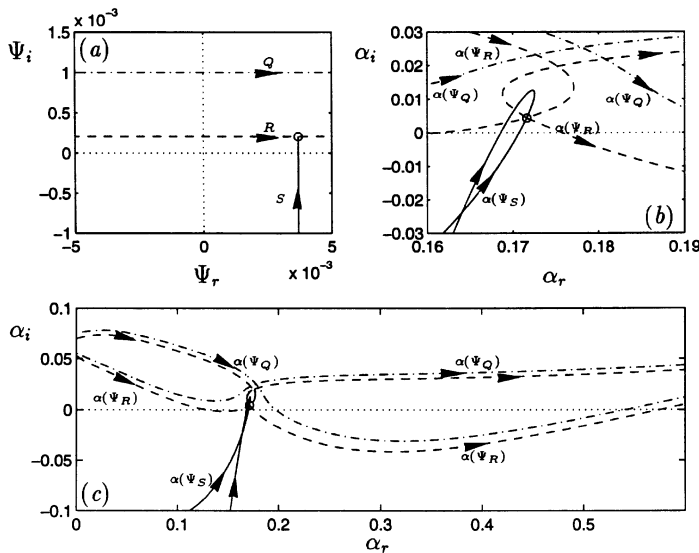


Figure 8. Mapping of the steepest-descent path from the  $\Psi$  to the  $\alpha$ -plane through a trajectory  $b$  saddle point for  $R = 460$ ,  $\beta = 20$  and  $(r - r_s)/t = 0$ : (a) the  $\Psi$ -plane, (b) expanded view of the  $\alpha$ -plane, (c) the  $\alpha$ -plane. The notation is the same as that for Figure 7.

the  $\alpha$ -plane for  $R = 460$ ,  $\beta = 20$ , and  $(r - r_s)/t = 0$ . All the notation is the same as that used to describe Figure 7. Figure 8b is an expanded view of the area around the saddle point shown in Figure 8c. Again, because  $(r - r_s)/t = 0$ , the  $\Psi$ -plane is equivalent to the  $\omega$ -plane and the two branches of  $\alpha(\Psi_R)$  are equivalent to branches 1 and 2 of the dispersion relation, which both originate in the upper half of the  $\alpha$ -plane and are denoted by  $\alpha_{1,2}(\omega_{F''})$  in Figure 9a of [2] (for different  $R$  and  $\beta$ ). Branch points between these two branches are not of pinch type.

Above the saddle point (see Figure 8b),  $\alpha(\Psi_R)$  loops round and crosses itself. At this intersection  $\alpha$  maps to two separate values of  $\Psi$ , which are on different Riemann sheets, and therefore there must be a value of  $\alpha$  within the loop that is a branch point of  $\Psi(\alpha)$ , and of  $\omega(\alpha)$ , where  $\partial\Delta_0/\partial\omega = \partial\alpha/\partial\omega = 0$  (the condition excluded in the previous discussion). The branch point is not shown in the figure, but it lies at  $\alpha \approx 0.172 + i0.0126$ . The associated branch cut is shown in Figure 6, where the branch point does indeed lie close to the trajectory  $b$  saddle point. Since the steepest-descent path also loops round and crosses itself, it too must pass around the branch point and onto the second Riemann sheet. Obviously, there is no choice of branch cut that the steepest-descent path would not cross. Because the steepest-descent method relies on being able to make  $\Psi(\alpha)$  analytic (possibly with the aid of branch cuts, as here) and then to formulate a single-valued analytic inverse function  $\alpha(\Psi)$ , it is not possible to deform the  $A$ -contour onto the steepest-descent path through a saddle point, such as the example given in Figure 8, for which the steepest-descent path describes a closed curve around a branch point of  $\Psi(\alpha)$ . It follows that branch points of the Riemann sheets are now important and the sheets can no longer be considered separately, as they are in (3.35)–(3.37). This result is consistent with Briggs' method, because a saddle point involving branches 1 and 2 would not be expected to give a singular integral such as Equation (3.37).

With the Fainberg–Kurilko–Shapiro method [23] for distinguishing between absolute and convective instability, which predates the Briggs' method, the various sheets of  $\omega(\alpha)$  are considered separately, with the implicit assumption that the bracketed term in Equation (3.36) is an entire function of  $\alpha$ , and the integration variable is changed from  $\alpha$  to  $\omega$  as in (3.36). From this process, it is concluded that if there is a saddle point of  $\omega(\alpha)$  corresponding to a value of  $\omega$  with positive imaginary part, there is an absolute instability. From the preceding discussion, it is clear that this procedure correctly identifies the absolute instability associated with a pinch point, but neglects the important consequences of a branch point of  $\omega(\alpha)$ . Thus, the Fainberg–Kurilko–Shapiro method would incorrectly identify the case given in Figure 8 as absolutely unstable, just as the steepest-descent method would, if used carelessly.

With the branch cut arbitrarily chosen as shown in Figure 6, the second Riemann sheet has no saddle points; the leading-order contribution given by the steepest-descent method for a path with end points in the same valley is of  $O(t^{-1})$ , i.e., higher order than the  $O(t^{-1/2})$  contribution from a path passing through a saddle point. Consequently, the dominant contribution for  $(r - r_s)/t = 0$  is given by the saddle-point contribution from the saddle point on trajectory  $a$  alone, shown in Figure 7.

As  $(r - r_s)/t$  varies, the behavior of the steepest-descent path through trajectory  $b$  saddle points changes in a way illustrated by the series of Figures 9–11. Figure 9 is for  $R = 460$ ,  $\beta = 20$ , and  $(r - r_s)/t = 0.04$ , where the behavior of the steepest-descent path is essentially the same as that for  $(r - r_s)/t = 0$ , except that the loop in the path is very much smaller (requiring an expanded view given by Figure 9c to be discernible). Furthermore,  $\alpha(\Psi_R)$  and  $\alpha(\Psi_Q)$  are influenced by the presence of the trajectory  $a$  saddle point, which is marked by  $+$ . Because the steepest-descent path must

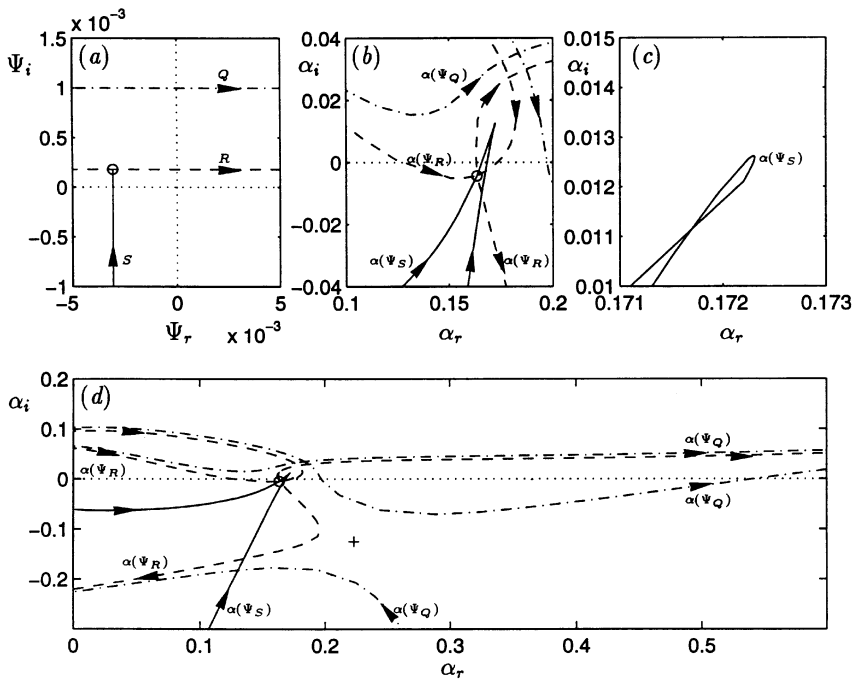


Figure 9. Mapping of the steepest-descent path from the  $\Psi$  to the  $\alpha$ -plane through the trajectory  $b$  saddle point for  $R = 460$ ,  $\beta = 20$ , and  $(r - r_s)/t = 0.04$ : (a) the  $\Psi$ -plane, (b) expanded view of the  $\alpha$ -plane, (c) more expanded view of the  $\alpha$ -plane, (d) the  $\alpha$ -plane. The notation is the same as that for Figure 7.

still cross any choice of branch cut from the branch point of  $\Psi(\alpha)$  enclosed by the small loop in the path, the  $A$ -contour cannot be deformed to pass through the saddle point.

Although Figure 10, which is for  $(r - r_s)/t = 0.06$ , looks very similar to Figure 9, the steepest-descent path does not cross itself, despite passing part way around the branch point, and therefore a branch cut can be chosen that is not crossed by the steepest-descent path and the path can lie on one analytic Riemann sheet. Accordingly, the  $A$ -contour can be deformed onto the steepest-descent path for this value of  $(r - r_s)/t$  and the  $\alpha$ -inversion has contributions from both trajectory  $a$  and  $b$  saddle points. Similarly, in Figure 11, which is for  $(r - r_s)/t = 0.1$ , the steepest-descent path does not cross itself and the  $A$ -contour can be deformed onto the steepest-descent path. Note, in Figures 10 and 11 the intersection of  $\alpha(\Psi_S)$  and  $\alpha(\Psi_R)$  does not imply that the steepest-descent path has passed out of the valley. The branch cut from the branch point puts  $\alpha(\Psi_R)$  at the intersection on the second Riemann sheet; therefore there is no real intersection, and  $\alpha(\Psi_S)$  remains in the low-ground relative to the branch of  $\alpha(\Psi_R)$  on its Riemann sheet.

For  $R = 460$  and  $\beta = 20$ , the  $A$ -contour can be deformed through trajectory  $b$  saddle points for values of  $(r - r_s)/t$  larger than about 0.05. For these  $(r - r_s)/t$ , the values of  $\Psi$  at the branch points are also pinch points of  $\alpha(\Psi)$ ; the two branches of  $\alpha(\Psi_R)$  originate in distinct halves of the

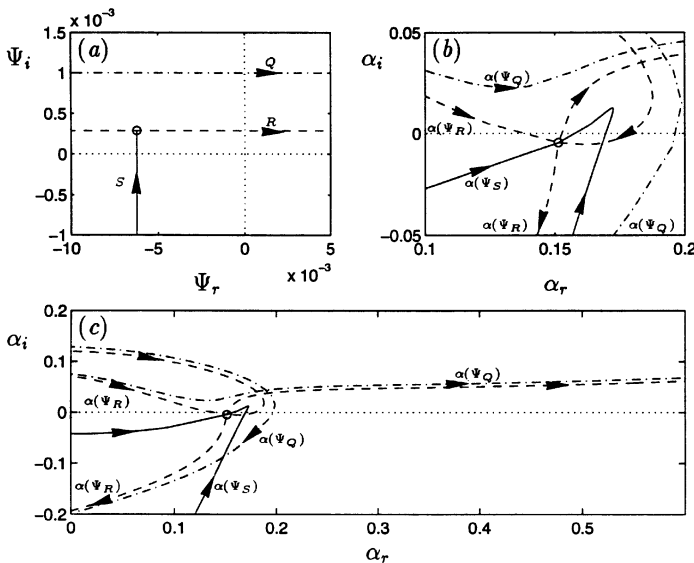


Figure 10. Mapping of the steepest-descent path from the  $\Psi$  to the  $\alpha$ -plane through the trajectory  $b$  saddle point for  $R = 460$ ,  $\beta = 20$ , and  $(r - r_s)/t = 0.06$ : (a) the  $\Psi$ -plane, (b) expanded view of the  $\alpha$ -plane, (c) the  $\alpha$ -plane. The notation is the same as that for Figure 7.

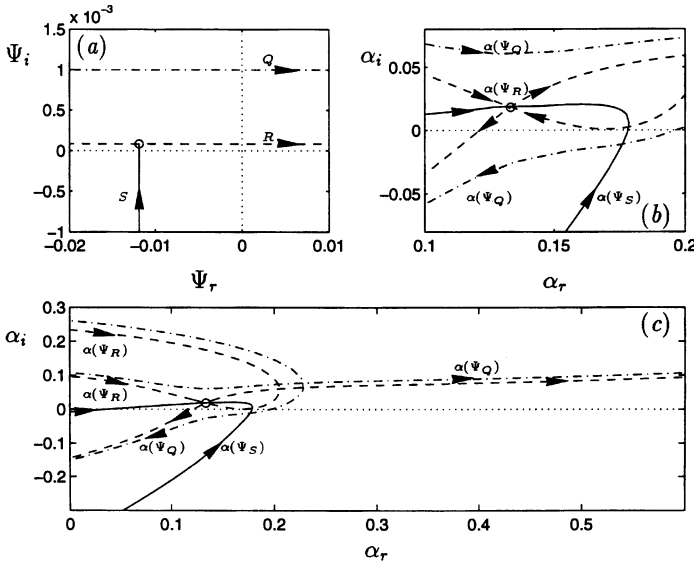


Figure 11. Mapping of the steepest-descent path from the  $\Psi$  to the  $\alpha$ -plane through the trajectory  $b$  saddle point for  $R=460$ ,  $\beta=20$ , and  $(r-r_s)/t=0.1$ : (a) the  $\Psi$ -plane, (b) expanded view of the  $\alpha$ -plane, (c) the  $\alpha$ -plane. The notation is the same as that for Figure 7.

$\alpha$ -plane for large positive  $\Psi_i$ . In Figure 5, the temporal growth rate  $\psi_r$  is positive on trajectory  $b$  below  $(r-r_s)/t \approx 0.11$ , but only those saddle points for  $(r-r_s)/t$  between about 0.05 and 0.11 are relevant.

## 4. Three-dimensional wave packets

### 4.1. Using the steepest-descent method

To obtain the wave-packet response in  $(r, \theta, t)$ -space to impulsive *point* forcing, it is necessary to perform a summation over all integer values of  $\beta$  that give amplified responses, which involves calculating the saddle-point trajectories as  $(r-r_s)/t$  varies for a large range of  $\beta$ . Because of the difficulty, discussed in the previous section, involved in establishing whether or not the  $A$ -contour can be deformed onto the steepest-descent path through trajectory  $b$  saddle points, the valid (as well as the invalid) contributions from saddle points on trajectory  $b$  are omitted here. In this section the wave packets are shown in the laboratory reference frame (denoted by the subscript  $l$ ). Note that this change of reference frame makes no difference to the important feature of radial absolute instability. The nondimensional

relationship between the laboratory and rotating frame is

$$\omega_1 = \omega + \bar{\beta}, \quad \theta_1 = \theta + \frac{t}{R}, \quad (4.1)$$

and therefore

$$e^{i(\alpha(r-r_s)+\beta\theta_1-\omega_1 t)} \equiv e^{i(\alpha(r-r_s)+\beta\theta-\omega t)}. \quad (4.2)$$

For calculation of a wave packet, the Reynolds number has been kept fixed, because within the context of the parallel-flow approximation, variations in the Reynolds number with respect to the radius are ignored. Clearly, when the approximation is applied over a large range of radii, as it is here, the approximation is poor. Ideally, as  $r$  varies, the appropriate Reynolds number would be used for the calculation of the terms in (3.28) that are dependent on  $R$ , e.g.,  $\alpha^*$ ,  $\omega^*$ , and  $\partial^2\omega/\partial\alpha^2$ . But this would involve calculating the saddle-point trajectories for a large range of  $R$  as well as all unstable  $\beta$ . As a compromise, saddle-point trajectories for all unstable  $\beta$  have been calculated for just two Reynolds numbers:  $R=400$ , in the convectively unstable regime, and  $R=550$ , in the absolutely unstable regime. These two examples show the qualitative differences between the two regimes.

For  $R=400$ , integer values of  $\beta$  between 0 and 85 are included in the  $\beta$ -summation. It is to be understood that the symmetric solutions (described at the beginning of Section 3.1) given by  $-\beta$  are automatically given by the  $+\beta$  solutions and are also included in the summation. Because of the amount of computation and storage required to calculate  $\Theta(z, \alpha^*)$ , in Equation (3.28), it is taken as unity for convenience, and for the reasons discussed above, the value of  $M$  in (3.28) is limited to 1, with only trajectory  $a$  saddle-point contributions included. Thus, from (3.28), the following series of figures represent

$$w(r, \theta_1, t) = \frac{H(t)}{2\pi} \sum_{\beta=0}^{85} \frac{e^{i(\alpha^*(r-r_s)+\beta\theta_1-\omega_1^* t)}}{[2\pi i t (\partial^2\omega_1/\partial\alpha^2)]_{\alpha^*, \omega_1^*}^{1/2}}, \quad (4.3)$$

where the physical solution is understood to be given by the real part of (4.3). For  $R=550$ , integer values of  $\beta$  between  $-11$  and  $135$  are included in the  $\beta$ -summation, again  $\Theta(z, \alpha^*)$  is taken as unity, and only trajectory  $a$  saddle-point contributions are included.

In Figure 12 the progression of three-dimensional wave packets is given for  $R=400$  and  $R=550$  at fixed times at equally spaced intervals. For clarity, only one positive (solid lines) and one negative (dotted lines) contour



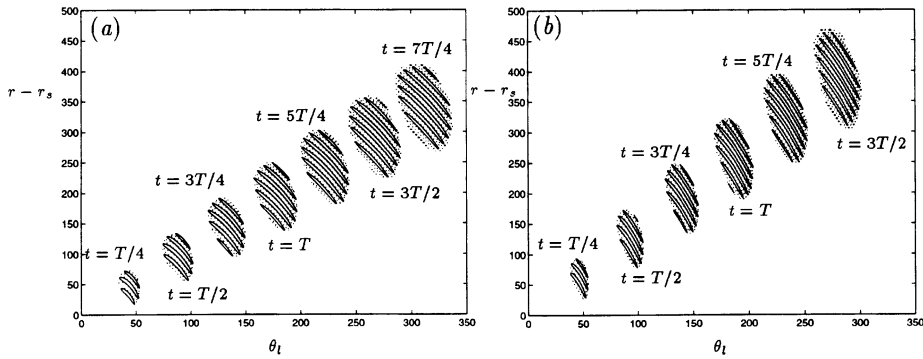


Figure 12. Progression of three-dimensional wave packets at fixed times: (a)  $R = 400$  and  $t$  increases from  $T/4$  and  $7T/4$  in steps of  $T/4$ , (b)  $R = 550$  and  $t$  increases from  $T/4$  to  $3T/2$  in steps of  $T/4$ , where  $T$  is the period of revolution of the disk.

level is shown; each packet is peak normalized and the contours plotted are  $\pm \frac{1}{6}$ . This figure shows that, in both cases, when the position of the source has rotated through, say, a quarter turn ( $t = T/4$ , where  $T$  is the period of revolution of the disk), the wave packet has moved through an angle of only about  $\theta_1 = 45^\circ$ . Thus, the wave packet lags behind the position of the source. The center of the packet moves through the same radial and angular displacement in each equal time interval, but the disturbed area increases because the front of the packet moves faster than the back.

Because  $R$  is constant for all  $r$ , the trajectory of the packet in this calculation is determined by the Reynolds number at the source. Thus, in Figure 12a, the behavior of the packet remains convective into regions now known to be absolutely unstable. Moreover, even with the source at a Reynolds number that gives absolute instability such as Figure 12b, where the progression of a wave packet is given for  $R = 550$ , the behavior appears convective. This is because, for a consistent comparison, the same contour levels as in Figure 12a are shown for each packet. Since the maximum value of  $|w(r, \theta, t)|$  occurs along a ray with positive  $(r - r_s)/t$  and is much larger than the amplitude at  $r = r_s$ , the chosen contour levels indicate convective rays. Figure 13 makes this point clearer. Of all the values of  $\beta$  included in the summation for  $R = 550$ , the growth rate  $\psi_r^*$  has its maximum value for  $\beta = 60$  at  $(r - r_s)/t \approx 0.75$  and the maximum absolute growth rate (necessarily at  $(r - r_s)/t = 0$ ) occurs for  $\beta = 75$ ; see Figure 13a. Figure 13b emphasizes the difference in the maximum convective and absolute growth rates; it takes about ten times as long for the amplitude at the source to grow to the same amplitude as the most convective part of the packet and at any particular time the amplitude at the source is a small proportion of the maximum amplitude within the wave packet. Nevertheless, after sufficient time the amplitude at the source will be big enough to cause nonlinearities

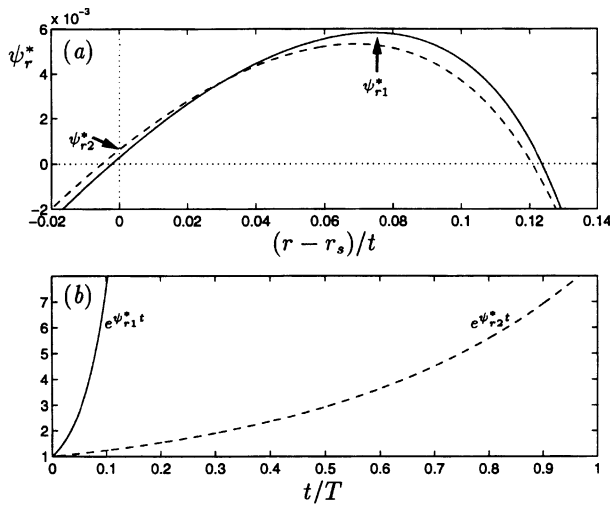


Figure 13. The maximum absolute growth rate compared to the maximum convective growth rate at  $R = 550$ : (a) saddle-point trajectories, i.e.,  $\psi_r^*$  against  $(r - r_s)/t$ , for  $\beta = 60$  (—) and  $\beta = 75$  (---), (b) the maximum convective exponential growth for  $\beta = 60$  (—), and the maximum absolute exponential growth for  $\beta = 75$  (---), against  $t/T$ .

and to fix the radial position of the onset of transition and the larger convective growth rates outward from the source will be modified by nonlinear behavior. However, if it can be assumed that some features of the linear results are applicable even once the flow has become nonlinear, these large convective growth rates may be important. At any particular radial position, outward from the source, the temporal growth rate approaches the absolute growth rate (i.e., the growth rate at the source, given by  $\omega_i^o$ ) as  $t \rightarrow \infty$ , but the disturbance always has a larger amplitude than that at the source because it went through a period of stronger growth at an earlier time as it crossed the ray with the maximum growth rate. This may explain why the flow is observed to become fully turbulent some way downstream from the position for the onset of transition (see [3]). In the words of Huerre and Monkewitz [24], the nonlinear global mode that results from a finite region of local absolute instability may be thought of as a highly repeatable “self-excited, low-amplitude, *wavemaker* ... , which acts as a source for the downstream instability wave(s).”

#### 4.2. Using numerical summation

Because of problems associated with the method of steepest descent, a numerical-summation method is used in this section, which is similar to that used by Gaster [20] for the Blasius boundary layer and by Spooner and Criminale [25] for the Ekman boundary layer, to illustrate the wave-packet

development for a single Reynolds number. The numerical-summation method does not involve making a time-asymptotic approximation and although the results do not apply at very small times, because the continuous spectra and most of the decaying modes are neglected, they do, in principle, apply at all other times. However, in practice, because of the parallel-flow approximation, which ignores the variation of Reynolds number with radius, the wave-packet development diverges from the true behavior as it propagates away from the source with increasing time.

As before, to find the discrete response to localized point forcing, the  $\omega$ -inversion is performed first using the residue theorem, giving Equation (3.23), and  $\Theta_j(z; \alpha)$  is taken as unity. Here, both unstable modes are included, i.e.,  $M = 2$ . Now, instead of deforming the  $A$ -contour onto a steepest-descent path to collect the dominant time-asymptotic contributions, the  $\alpha$ -integral is approximated by a Fourier series, giving the vertical perturbation velocity as

$$w(r, \theta, t) \simeq \frac{H(t)}{(2\pi)^2 i} \sum_{\beta=-\infty}^{+\infty} \sum_{\alpha=-\infty}^{+\infty} \sum_{j=1}^M e^{i(\alpha(r-r_s) + \beta\theta - \omega_j(\alpha)t)}, \quad (4.4)$$

and evaluated numerically. Here  $\beta$  has integer values, as usual, and  $\alpha$  is real, representing the integration along the  $A$ -contour lying on the real axis, and the physical solution is understood to be given by the real part of (4.4). The solution in the laboratory frame,  $w(r, \theta_1, t)$ , is easily calculated from (4.4) using Equations (4.1) and (4.2).

The initial disturbance excites all possible modes of behavior but, in practice, the  $\alpha$ - and  $\beta$ -summations are limited to ranges that include all the unstable responses, i.e., those giving positive values of  $\omega_i$ . The neglect of most of the damped modes and the continuous spectra causes inaccuracies in the wave-packet representation at short times after the inception of the disturbance, before the damped modes have had a chance to die away. Figure 14 shows contours of  $\omega_i$  given by real  $\alpha$  and  $\beta$  for  $R = 300$ . The lowest contour represents  $\omega_i = 0$  and they increase in steps of 0.0005 up to  $\omega_i = 0.0025$ . The  $\beta$ -summation in (4.4) ranges from  $\beta = -60$  to  $\beta = 45$  and the  $\alpha$ -summation includes values of  $\alpha$  from 0 to 0.5. It is to be understood that the summations also include values of  $\omega$  given by the symmetric modes, i.e., those given by  $-45 \leq \beta \leq 60$  and  $-0.5 \leq \alpha \leq 0$ , for which  $\omega_r$  is the negative of that given by the original ranges and  $\omega_i$  is the same. With reference to Figure 6 of [2] (which shows neutral-stability curves for a range of frequencies) at  $R = 300$ , it is clear that the small island of unstable eigenvalues, with more positive  $\beta$  and relatively large  $\alpha$ , corresponds to inviscid modes (which remain unstable as  $R \rightarrow \infty$ ) denoted by branch 1, while

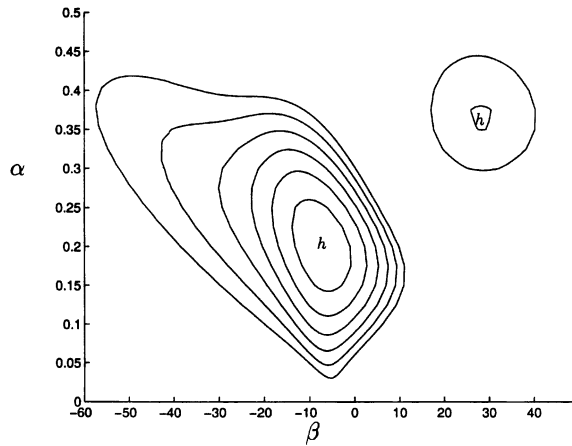


Figure 14. Contour plot of  $\omega_i$  for  $R=300$  and real  $\beta$  and  $\alpha$ . The high ground is marked by  $h$ .

the large island, with mostly negative  $\beta$  and generally smaller  $\alpha$ , corresponds to viscous modes (which have no inviscid counterpart) denoted by branch 2.

Again from Figure 6 of [2], it can be seen that the wave angles of the two islands of growing modes are distinct: The branch 1 island is associated with relatively large positive wave angles, while the branch 2 island has smaller positive and negative wave angles. Therefore, the wave packets formed from the summation of modes in the two islands should have their wave fronts oriented in different directions. Furthermore, at  $R=300$ , Figure 14 suggests that, although branch 1 is more unstable than branch 2 for stationary waves and waves with negative  $\omega_r$  (in fact, for these frequencies, branch 2 is damped for Reynolds numbers below about 460), the destabilizing effect of positive  $\omega_r$  on branch 2 results in the largest growth rates. As the Reynolds number increases, the destabilizing effect on branch 1 of negative  $\omega_r$  becomes more important, causing maximum growth rates larger than branch 2; but branch 2 contributions are important to the development of disturbances at Reynolds numbers relevant to the unstable region leading up to transition, and their omission from the steepest-descent wave packets is a poor approximation.

There is a strong similarity in results between a study by Spooner and Criminale [25] of the evolution of disturbances originating from an initially localized pulsed perturbation at the boundary in the Ekman boundary layer, using numerical summation, and those from this analysis of the rotating-disk boundary layer. Both studies describe the presence of two modes of instability: a viscous mode (referred to by Lilly [26] as the parallel mode) that

dominates at low Reynolds numbers and an inviscid mode that dominates at higher Reynolds numbers, with an intermediate range where both modes are unstable, as they are for  $R = 300$  in the rotating-disk boundary layer.

For nondimensional times between  $t = 25$  and  $t = 1000$ , the evolution of the initial disturbance is represented in Figure 15. At  $t = 25$ , the wave packet is still very pulse-like, but by  $t = 100$  the two maxima in Figure 14 are represented in the developing wave packet, with the disturbance taking the

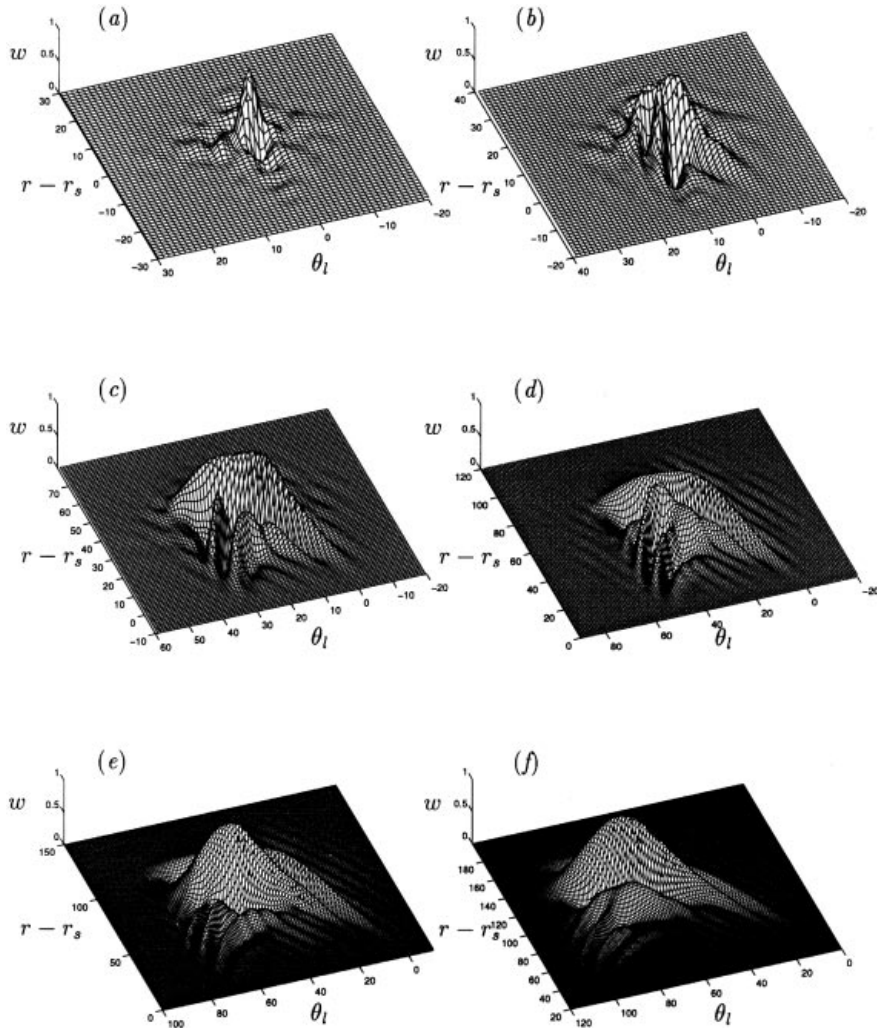


Figure 15. Perspective plot of  $w(r, \theta_l, t)$  for  $R = 300$ : (a)  $t = 25$ , disk moved through about  $5^\circ$ , (b)  $t = 100$ , disk moved through about  $19^\circ$ , (c)  $t = 300$ , disk moved through about  $57^\circ$ , (d)  $t = 500$ , disk moved through about  $95^\circ$ , (e)  $t = 700$ , disk moved through about  $134^\circ$ , (f)  $t = 1000$ , disk moved through about  $191^\circ$ .

form of two overlapping packets. The smaller packet, which is characterized by a slightly larger angular position and positive wave angle, represents the inviscid modes (branch 1). These are the only contributions included in the steepest-descent wave packets, in Figure 12 (the view in Figure 15 is chosen to render the smaller packet visible in front of the larger packet, meaning that  $\theta_1$  increases from right to left rather than left to right as in Figure 12). The larger packet corresponds to the viscous modes (branch 2), having negative wave angle. The dominant component of the two packets is given by the maxima of Figure 14. In common with the competing instabilities in the Ekman boundary layer, the two packets remain essentially together, creating a single patch of disturbance, which contains two overlapping packets that spread in time. This implies that the group velocities of the two packets are similar. The experimental results discussed in [3] also show the two components of the wave packet in the convectively unstable regime.

As discussed by Spooner and Criminale [25], a signal represented by a series of the form  $\sum_n^N \cos(a_o + n \Delta a)x$ , such as the Fourier series in (4.4), are aliased over a distance of  $2\pi/\Delta a$ . For the  $\alpha$ -series, the step-size is 0.005, giving aliasing over a radial distance of about 1256, and for the  $\beta$ -series the step-size is 1, which gives aliasing over an angle of  $2\pi$ . Clearly, it is desirable to restrict the perspective plots to lie within these regions, to prevent distortion by aliasing. Another source of inaccuracy of this solution scheme is the representation of the integrals by truncated series. The truncation produces ringing (a general feature of a rectangular Fourier spectrum), especially at short times after the initiation of the pulse. For example, in Figure 15a, small amplitude waves that appear to propagate outward from the wave packet are clearly visible, but these distortions decrease with increasing time as growth of the amplitude coefficients smoothes the ends of the Fourier spectrum. A Hann-window function [27] was applied, in both the radial and circumferential direction, to the data plotted in Figure 15 to create a smoother effect around the edges of the wave packets.

In common with the evaluation of wave packets using the method of steepest descent, the variation of Reynolds number with radius has been ignored; the wave-packet development has been treated in an analogous way to the development in the truly parallel Ekman boundary layer presented by Spooner and Criminale [25]. The Ekman boundary layer is free from the parallel-flow approximation because, although similar to the rotating-disk flow, it is a strictly parallel flow, both in the physical sense and in the sense that the Reynolds number is independent of distance; the governing equations are separable without any approximation. Because of the parallel-flow approximation in the rotating-disk analysis, there is an increasing discrepancy between the true wave-packet development with time and that given in Figure 15. However, it is likely that the qualitative features in Figure 15 are representative of the real wave-packet evolution at small distances from the source.

It would be possible to calculate more accurate representations of the wave-packet development by employing the techniques used by Gaster [20]. Gaster used a direct numerical-summation scheme to calculate the wave-packet development in the Blasius boundary layer, which grows in the downstream direction. In the study, the parallel-flow assumption was made and the discrete spectrum was represented by a sum of normal modes (as here, the continuous spectra were neglected). Eigenvalues from the single unstable mode were calculated at Reynolds numbers appropriate to all the streamwise ( $x$ ) locations used in the accompanying experiment, such that the disturbance at a particular  $x$ -position, spanwise location  $z$  and time, has the form

$$\sum_{\omega} \sum_{\beta} e^{i(\int_{x_s}^x \alpha(x; \omega, \beta) dx + \beta z - \omega t)}. \quad (4.5)$$

If a quasi-nonparallel correction of this sort were applied to the rotating-disk problem, the data in Figure 14 would have to be calculated for a series of closely spaced Reynolds numbers. The range of unstable circumferential wavenumbers increases rapidly with increasing Reynolds number (at  $R = 500$ ,  $\beta$  is unstable between about  $-80$  and  $120$ , compared with the range of  $-60$  to  $40$  at  $R = 300$ ), which means, if the  $\alpha$ -interval remains  $0.005$ , then for just six radial positions about  $91500$  eigenvalues (based on the number of unstable wavenumbers averaged between  $R = 300$  and  $R = 500$ ) would be required, compared to Gaster's stated total of  $8000$  ( $24$   $x$ -positions were used, personal communication 1995). Clearly, this procedure would involve considerable computing time and has not yet been attempted for the rotating-disk flow.

## 5. Conclusions

Because the steepest-descent method is well known, it is tempting to use the standard textbook solution for the  $\alpha$ -inversion, without investigating the global topography of the phase function, but this has been shown to be a dangerous course. The examples given in Section 3.1.2 show that not all saddle points of the phase function are relevant to the  $\alpha$ -inversion. The specific examples where  $(r - r_s)/t = 0$  are relevant to all flows, because for this ray the phase function  $\psi(\alpha)$  is a simple rotation of  $\omega(\alpha)$ , the saddle points of the phase function are also saddle points of the dispersion relation and there is a direct correspondence between Briggs' criterion and whether the steepest-descent path can pass through the saddle point. As mentioned by Huerre and Monkewitz [24], the important conclusion from the discussion of the steepest-descent method is that the ray of  $(r - r_s)/t = 0$  only indicates absolute instability if  $\omega_i^*$  is positive and  $\omega^*$  is a pinch point of  $\alpha(\omega)$ .

Further, for other values of  $(r - r_s)/t$ , saddle-point contributions are only relevant if the coalescing branches of  $\alpha(\Psi)$  originate in distinct half-planes for large positive  $\Psi_i$ , i.e., if the branches pinch the steepest-descent path.

The discussion of the steepest-descent method highlights the fact that the various sheets of  $\omega(\alpha)$  cannot always be considered separately, because branch points of  $\omega(\alpha)$  play an important role in the steepest-descent inversion. This point is not well documented. For instance, Gaster [14, 17] studies impulsive point-source excitation and the time-asymptotic solution is assumed to depend on the  $\omega$ -inversion of the exponential term alone, with the assumption that all other terms are entire functions. This is not the case (see Equation (3.36)), because  $\partial\Delta_0/\partial\omega$  always has at least one zero [21] and saddle-point contributions should only be included if the steepest-descent path does not encircle the value of  $\alpha$  at this zero, which it does when the coalescing branches of  $\alpha(\Psi)$  do not pinch. As discussed, the same oversight causes the failure of the Fainberg–Kurilko–Shapiro criterion for absolute instability. Nonetheless, careful use of the method of steepest descent can give the time-asymptotic form of the wave packet that develops from point-source excitation. The results for the absolutely unstable case show that even at a Reynolds number about 8% higher than the critical value for the onset of absolute instability, the absolute growth rate is significantly smaller than the maximum growth rate further downstream. But, in the context of linear theory, the amplitude at the source continues to grow indefinitely although, in reality, the temporal growth is bounded by nonlinear behavior. Assuming that the local absolute instability causes a nonlinear global mode, the latter can be thought of as a self-excited source of disturbances that continue to grow in time at all positions downstream.

If implementation of the steepest-descent method proves to be difficult, then more satisfactory representations of the wave-packet development are found using numerical summation to approximate the  $\alpha$ -inversion. Using this method, both instability modes are included without difficulty, showing that at lower Reynolds numbers the traveling disturbances given by the viscous modes (branch 2) are more unstable than those from the inviscid modes (branch 1), but it can be shown that for Reynolds closer to 500, and above, the inviscid mode is more unstable.

Theoretically, the numerical-summation method described in Section 4.2 is applicable at all times apart from at very short times after the initiation of the pulse, when the continuous spectra and all the damped discrete modes are important. However, because of the parallel-flow approximation, as time increases, the packet development diverges from the true behavior in the boundary layer. The wave-packet evolution at the chosen Reynolds number of 300 is shown to be very similar to that of the evolution in the Ekman boundary layer at intermediate Reynolds numbers [25]. In common with the competing instabilities in the Ekman boundary layer, two wave packets that



remain together are created by the localized pulsed perturbation at the boundary, creating a single patch of disturbance, in which the two packets overlap and spread in time.

Although the method of numerical summation can be a satisfactory way of illustrating the wave-packet development, it would be a very inelegant method of determining whether the instability is convective or absolute. Briggs' method is far less time consuming, because for each Reynolds number it is necessary only to search for branch points of  $\alpha(\omega)$  (a condition that can be incorporated into the eigenvalue solver; i.e., the code can be made to shoot for solutions of the boundary conditions and simultaneous zeros of  $\partial\omega/\partial\alpha$ ) and, importantly, to check that in the limit of large positive  $\omega_i$  the branches of  $\alpha(\omega)$  that coalesce at the branch point lie in distinct halves of the  $\alpha$ -plane.

### Acknowledgment

This work was completed while the author was supported by a Research Fellowship at Pembroke College, Cambridge.

### References

1. TH. VON KÁRMÁN, Über laminare und turbulente Reibung, *Z. Angew. Math. Mech.* 1:233 (1921).
2. R. J. LINGWOOD, Absolute instability of the boundary layer on a rotating disk, *J. Fluid Mech.* 299:17 (1995).
3. R. J. LINGWOOD, An experimental study of absolute instability of the rotating-disk boundary-layer flow, *J. Fluid Mech.* 314:373 (1996).
4. R. J. BRIGGS, *Electron-Stream interaction with Plasmas*, Chap. 2, MIT Press, 1964.
5. D. E. ASHPIS and E. RESHOTKO, The vibrating ribbon problem revisited, *J. Fluid Mech.* 213:531 (1990).
6. M. GASTER, On the generation of spatially growing waves in a boundary layer, *J. Fluid Mech.* 22:433 (1965).
7. L. H. GUSTAVSSON, The initial-value problem for boundary layer flows, *Phys. Fluids* 22:1602 (1979).
8. K. KUPFER, A. BERS, and A. K. RAM, The cusp map in the complex-frequency plane for absolute instabilities, *Phys. Fluids* 30:3075 (1987).
9. H. SALWEN and C. E. GROSCH, The continuous spectrum of the Orr-Sommerfeld equation. Part 2. Eigenfunction expansions, *J. Fluid Mech.* 104:445 (1981).
10. P. R. BRAZIER-SMITH and J. F. SCOTT, Stability of fluid flow in the presence of a compliant surface, *Wave Motion* 6:547 (1984).
11. D. J. BENNEY and L. H. GUSTAVSSON, A new mechanism for linear and nonlinear hydrodynamic instability, *Stud. Appl. Math.* 64:185 (1981).
12. W. KOCH, Direct resonance in Orr-Sommerfeld problems, *Acta Mech.* 58:11 (1986).

13. D. S. HENNINGSON, A. LUNDBLADH, and A. V. JOHANSSON, A mechanism for bypass transition from localized disturbances in wall-bounded shear flows, *J. Fluid Mech.* 250:169 (1993).
14. M. GASTER, The development of three-dimensional wave packets in a boundary layer, *J. Fluid Mech.* 32:73 (1968).
15. M. GASTER, Propagation of linear wave packets in laminar boundary layers, *AIAA J.* 19:419 (1981).
16. M. GASTER, Estimates of errors incurred in various asymptotic representations of wave packets, *J. Fluid Mech.* 121:365 (1982).
17. M. GASTER, The development of a two-dimensional wave packet in a growing boundary layer, *Proc. R. Soc. London Ser. A* 384:317 (1982).
18. P. HUERRE and P. A. MONKEWITZ, Absolute and convective instabilities in free shear layers, *J. Fluid Mech.* 159:151 (1985).
19. L. M. MACK, The wave pattern produced by point source on a rotating disk, *AIAA Paper* 85-0490 (1985).
20. M. GASTER, A theoretical model of a wave packet in the boundary layer on a flat plate, *Proc. R. Soc. London Ser. A* 347:271 (1975).
21. M. GASTER, Growth of disturbances in both space and time, *Phys. Fluids* 11:723 (1968).
22. H. JEFFREYS, *Asymptotic Approximation*, pp. 18–25, Oxford Univ. Press, 1962.
23. YA. B. FAINBERG, V. I. KURILKO, and V. D. SHAPIRO, Instabilities in the interactions of charged particle beams with plasma, *Soviet Phys.—Tech. Phys.* 6:459 (1961).
24. P. HUERRE and P. A. MONKEWITZ, Local and global instabilities in spatially developing flows. *Ann. Rev. Fluid Mech.* 22:473 (1990).
25. G. F. SPOONER and W. O. CRIMINALE, The evolution of disturbances in an Ekman boundary layer, *J. Fluid Mech.* 115:327 (1982).
26. D. K. LILLY, On the instability of Ekman boundary flow, *J. Atmos. Sci.* 23:481 (1966).
27. W. H. PRESS, S. A. TEUKOLSKY, W. T. VETTERLING, and B. P. FLANNERY, *Numerical Recipes*, p. 547, Cambridge Univ. Press, 1992.

UNIVERSITY OF CAMBRIDGE

(Received February 16, 1996)